LBL-30132

Lawrence Berkeley Laboratory
UNIVERSITY OF CALIFORNIA

APPLIED SCIENCE DIVISION

Experimental and Theoretical Investigation of a Zinc Model Pore with Probe Beam Deflection

J.K. Weaver*, F.R. McLarnon, and E.J. Cairns
(*M.S. Thesis)

December 1990

APPLIED SCIENCE DIVISION

LOAN COPY
Circulates
for 2 weeks
Bldg. 50 Library.
LBL-30132
Copy 2

Prepared for the U.S. Department of Energy under Contract Number DE-AC03-76SF00098.

DISCLAIMER

This document was prepared as an account of work sponsored by the United States Government. While this document is believed to contain correct information, neither the United States Government nor any agency thereof, nor the Regents of the University of California, nor any of their employees, makes any warranty, express or implied, or assumes any legal responsibility for the accuracy, completeness, or usefulness of any information, apparatus, product, or process disclosed, or represents that its use would not infringe privately owned rights. Reference herein to any specific commercial product, process, or service by its trade name, trademark, manufacturer, or otherwise, does not necessarily constitute or imply its endorsement, recommendation, or favoring by the United States Government or any agency thereof, or the Regents of the University of California. The views and opinions of authors expressed herein do not necessarily state or reflect those of the United States Government or any agency thereof or the Regents of the University of California.

LBL-30132

EXPERIMENTAL AND THEORETICAL INVESTIGATION OF A ZINC MODEL PORE WITH PROBE BEAM DEFLECTION

by

Jeffrey Weaver, Frank R. McLarnon and Elton J. Cairns

Applied Science Division
Lawrence Berkeley Laboratory
University of California
Berkeley, California 94720

This work was supported by the Assistant Secretary for Conservation and Renewable Energy, Deputy Assistant Secretary for Utility Technologies, Office of Energy Management, Advanced Utility Concepts Division of the U.S. Department of Energy under Contract No. DE-AC03-76SF00098.

Experimental and Theoretical Investigation of a Zinc Model Pore with Probe Beam Deflection

by

Jeffrey Weaver

Abstract

Optical probe beam deflection has been employed to study two-dimensional concentration gradients within the electrolyte of a zinc model pore. The model pore cell constructed for this study retains the small, confined geometry and two-dimensional character of an actual pore within a porous zinc electrode. The concentration and concentration gradients of the electrolyte species were calculated by a numerical model and were used to interpret the experimental measurements obtained using the probe beam deflection technique. Good quantitative agreement between experiment and theory was obtained. The combination of theoretical and experimental analyses led to an understanding of how the kinetic, geometric, and mass transport parameters determined the current and concentration distributions within the model pore electrolyte.

Acknowledgements

I would like to thank Dr. Elton Cairns and Dr. Frank McLarnon who patiently directed my research. They also convinced me that secondary zinc cells should play an important role in the world's energy future, and thus left me with the belief that my work had some meaning apart from its pedagogic value.

Next, I would like to thank Jim Rudnicki and Ken Miller, who played major roles in my education. Without the help of these two fellow graduate students, my time at Berkeley would have been much less rewarding. Anyone who has worked in our research group during the last few years recognizes that Jim has played an important role in much of the work that was accomplished here. Ken provided extra help in explaining numerical modelling and secondary battery design.

Many other coworkers and members of Team Destructo added extra zest to my stay here. Thanks to Bruce, Hubert, Paul, Kathy, Mark I., Gessie, Stuart, Huey, Rick, Jon, Dave, Mark S., Ron, Wing Tat, Dorys, Jordan, Stefan, and Rosemary for sharing some humor and adventure. I will always remember the mountain biking, frisbee, sailing, camping, darts, golf, and stimulating lunch discussion. Without these activities and friends to complement my technical experience at Berkeley, I might not have had the perseverance to finish this thesis.

There are others from outside the research group who deserve some credit. So, additional thanks to Vance, Dan, Sue, Lesley, Yogi, Joel, Stacy, Jim Rose and many others, who gave me technical and recreational advice. Finally, my parents and sister deserve special thanks for giving me much more unquestioning support than I deserved.

This work was supported by the Assistant Secretary for Conservation and Renewable Energy, Deputy Assistant Secretary for Utility Technologies, Office of Energy Management, Advanced Utility Concepts Division of the U.S. Department of Energy under Contract No. DE-AC03-76SF00098.

Table of Contents

Chapter I Introduction 1

A. Motivation for this Study 1

B. The Model Pore as an Abstraction of an Actual Pore 2

Chapter II Experimental Approach and Results 7

A. The Optical Probe Beam Deflection Method 7

B. Equipment & Methods 11

1. Detection System 11

2. Structure of the Cell 14

3. Description of Experiments 19

C. Results 23

D. Summary & Conclusions 38

Chapter III Theoretical Analysis and Discussion 39

A. Motivation for the Numerical Model 39

B. Development of the Single-Pore Model 45

1. The Zinc Electrode 45

2. Mass Transfer 46

3. Transfer Current Density Distribution 49

4. Solution Technique 53

C. Comparison of Experimental and Theoretical Results 54

D. Summary & Conclusions 68

References 70

Appendix I: Refractive Index Measurements 76

Appendix II: Current Distribution Model 81

Appendix III: Mass-transfer Model 101

Chapter I Introduction

A. Motivation for this Study

Processes occurring within the pores of a porous electrode dictate the performance of many electrochemical systems. However, little work has been undertaken to characterize mass transfer processes within individual pores. For this reason, we have conducted a study of various processes occurring within an electrode pore. The cell used for these studies is a small model pore designed to simulate a single microscopic pore within a macroscopic porous electrode. The porous zinc electrode was chosen for this work because it is the negative electrode in a number of batteries under development for commercial applications. One major obstacle to widespread deployment of rechargeable zinc batteries is poor cycle life resulting from zinc redistribution and dendrite shorting, both of which are mediated by soluble zincate ion transport.

The ultimate disposition of electroactive species within a pore is expected to be strongly influenced by mass transfer. The mass transfer processes within a pore include diffusion, migration, and convection. Unravelling the contributions of these effects as well as other processes in an electrolyte is not trivial. This is especially true when, as with zinc electrodes, the supporting electrolyte reacts at the electrode. Even in a semi-infinite medium, determining the flux and concentration of the electroactive species near an electrode is a complicated problem often resisting analytical solution. In the microscopic domain of a single pore, the problem is exacerbated. Thus, an *in situ* technique for monitoring

concentration gradients within a working porous electrode or simulated pore would be useful in understanding the microscopic processes which underlie the performance of porous electrodes.

Electrode processes are typically studied in excess electrolyte where the concentration of soluble species remains nearly time invariant at locations far from the electrode. Thus, the concentration profiles in these systems are influenced by a very large sink or source for the reacting species. This situation should not be expected in a pore where a relatively small electrolyte volume is accessible to the surrounding electrode. Pores in zinc electrodes have been estimated to range in diameter from 1 to 40 μm, and have an average tortuosity of approximately 2 (1). Since the diffusion layer thickness grows as the square root of the product of the diffusion coefficient and the time of current passage (2), it should advance through the entire pore within a second. Thus, the more traditional macroscopic approaches to studying electrode processes quickly lose their applicability to processes occurring within an actual pore. However, a model pore cell provides a unique domain of chemical reactions and processes, unavailable in macroscopic electrode studies. Within a model pore, the concentrations, pH, current distribution, and other features should more accurately reflect the conditions found within an actual porous electrode.

B. The Model Pore as an Abstraction of an Actual Pore

The model pore used in this study is an abstraction of a real pore. The geometry chosen for this study is a rectangular slot having electrolyte sandwiched between two faces: one containing two planar zinc electrodes

and the other being an insulator. The levels of abstraction used to transform an actual electrode pore into the idealized cell employed here are set forth in Fig. 1. As shown in Fig. 1, the model pore can be viewed as a two-dimensional single pore sliced in half along its axis and having tortuosity equal to 1. Alternatively, the idealized pore might be viewed as a cylindrical pore which has been unwound in such a manner that its axis becomes an insulating plane and the cylindrical pore wall becomes a planar electrode.

These levels of abstraction are necessary to permit careful observation and treatment of the processes occurring within the pore. Because the electrolyte within a real pore is almost completely surrounded by opaque material, it is not amenable to optical observation. If, as is the case here, the model pore is to be probed by beam deflection techniques, the cell must deviate from an exact replication to accommodate observation. Thus, the model pore sides have been made transparent to permit a laser probe beam to graze the electrode surface. Although the model pore cell deviates from a real pore in some regards, it retains other important characteristics. First, the ratio of pore radius to average current density (per unit of pore wall area) is approximately retained. Thus, the diffusion layer grows throughout the whole cell quickly, as expected in an actual pore. Second, the idealized pore simulates two dimensions of an actual pore. Thus, mass transfer is occurring (and being monitored) simultaneously in directions normal to the pore wall and along the pore axis, i.e. parallel to the pore wall.

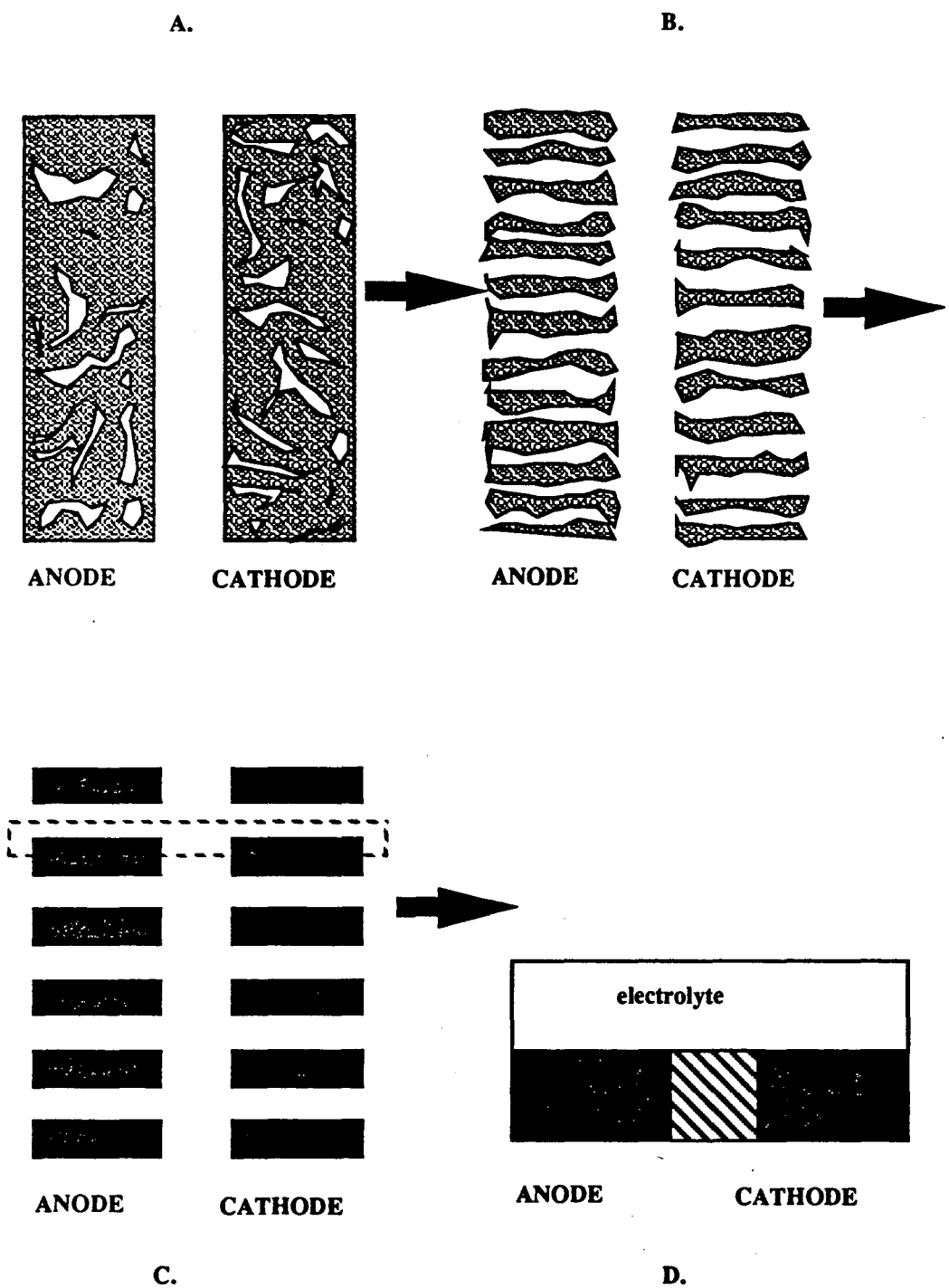

Figure 1. Pores are shown as they might appear in an actual electrode, A, having a network of randomly directed macropores interspersed in a microporous matrix. In B, the macropores have been directed so that they span the width of the electrode. In C, the tortuosity of the pores has been set equal to 1. Finally, D shows the actual configuration of the model macropore cell.

The model single pore used in this study is similar to a design originated by T. Katan, but modified for this study to allow measurement of concentration gradients (3). Katan *et al.* observed the progress of electrochemical reactions within a model zinc pore *in situ* by using optical microscopy. Like the cell used in this study, the cell used by Katan *et al.* essentially consisted of a thin alkaline electrolyte layer on top of zinc working and counter electrodes. To permit visual observation of the cell, a microscope slide served as the upper boundary of their cell. With this system, Katan *et al.* conducted galvanostatic experiments having volumetric current densities[1] ranging from 1.2 to 4.8 A/cm^3. With such high currents, they were able to observe hydrogen evolution, dendrite formation, flocculating precipitation, and ultimately passivation. They described "fronts" of oxidation product moving through the cell during the course of the reaction, noting morphological changes on the electrode. Aside from visual observation of the flocculating precipitate, however, Katan *et al.* did not directly observe or characterize the processes occurring within the pore electrolyte. Flatt *et al.* also investigated an alkaline zinc model pore with optical microscopy (1). In addition, they attempted to characterize the processes occurring within the electrolyte by using a series of cadmium reference electrodes spaced along the length of the pore. Their

---

[1] The volumetric current density in a model pore is given by the total cell current divided by the electrolyte volume adjacent to the working electrode. The volumetric current density for an actual pore is found by dividing the total cell current by the product of the electrode porosity and the electrode volume.

work included experiments at a wide range of volumetric current densities (0.1 A/cm^3 to 4.0 A/cm^3), some of which are comparable to those expected in the zinc electrode of a secondary battery. By measuring reference-electrode potentials at various locations along the length of the cell they arrived at a one-dimensional current distribution and proposed a plausible concentration distribution within the pore.

Chapter II Experimental Approach and Results

A. The Optical Probe Beam Deflection Method

Various techniques have been used to investigate concentration profiles at the electrode-electrolyte interface. Interferometry is commonly used for this purpose (4). In interferometry, phase variations in transmitted light are measured and the corresponding variations in refractive index - and ultimately concentration - are then derived. This technique permits simultaneous observation of both the concentration and the concentration gradient adjacent to an electrode. However, interferograms generated by this procedure are difficult to interpret, requiring careful consideration of beam deflection and reflection as well as the interference fringe pattern (5).

Techniques based upon optical absorption by colored solute species have also been employed to study concentration variations adjacent to electrodes. For example, Jan *et al.* (6) studied the electrochemical generation of trianisylamine cation radical ($TAA^{\cdot+}$) which absorbs light at the He-Ne laser beam wavelength. By passing the He-Ne beam through the electrolyte and them expanding the beam onto a photodiode array, the concentration profile of $TAA^{\cdot+}$ was obtained. Each pixel of the detector monitored the beam intensity passing by the electrode at a particular distance from the surface, with a reported resolution of better than 5 μm. Such techniques offer the advantage of selectivity for a particular component when more than one species is involved in an electrode reaction.

However, relatively few systems can be studied by these techniques because one solute species must absorb radiation at the probe beam wavelength. They also suffer from resolution degradation when the beam is bent by refractive index gradients unless small electrodes and small concentration gradients are used.

The technique employed in this study, optical probe beam deflection, responds to ionic concentration gradients generated near an electrode face. The principles underlying this technique have been described by Russo *et al.* (7) for a macroscopic cell using an alkaline copper system. The authors of that paper used a related technique known as photothermal deflection spectroscopy (PDS) which measures oscillating temperature gradients as well as concentration gradients in the electrolyte. Probe beam deflection techniques have been used or proposed by other investigators to observe concentration gradients in electrochemical systems (8,9,10). However, no reported work has yet applied this technique to electrochemical processes occurring in thin slots or other confined geometries, nor has there been work done on alkaline zinc systems.

Optical probe beam deflection works on the principle that a refractive index gradient in a transmitting medium deflects a light beam (usually a low-power laser beam) due to the Schlieren effect. When the refractive index and the refractive index gradient of a solution are invariant over the

region traversed by the laser beam[2], the expression for beam deflection in one dimension reduces to the following simple relationship:

$$\theta = \frac{l}{n_0} \cdot \frac{\partial n}{\partial y} \qquad [1]$$

Here, θ is a one-dimensional component of the angular deflection of the probe beam, l is the distance the beam travels in the electrolyte, n_0 is the average refractive index over the path traversed by the probe beam, and $\frac{\partial n}{\partial y}$ is the one-dimensional refractive index gradient in the electrolyte.

Equation 1 does not completely represent the measured deflection because the probe beam is further refracted when it passes through the cell exit window. Thus, the measured angle includes contributions from refraction at the cell window as well as refraction within the electrolyte. When the additional window refraction is taken into account and when θ is a small angle, Eq. 1 further simplifies to the following expression:

$$\theta_{obs} = l \cdot \frac{\partial n}{\partial y} \qquad [2]$$

---

[2] These assumptions are reasonable for the system used in this work. The calculated concentration differences for a typical experiment suggest that the total change in refractive index across the cell height is no more than 0.02%. Further, the beam deflection within the cell is typically of order 40μm which is small compared to the region over which the refractive index gradient is expected to change significantly.

As written, Eq. 1 and Eq. 2 apply to one-dimensional refractive index gradients only. However, the current distribution within the model pore varies in two dimensions. Thus, the direction of beam deflection will not be normal to the electrode (unlike the situation in most probe beam deflection studies) and will, in fact, vary within the model pore at different positions. The detection system must therefore separate the deflection angle into two components: one normal to the model pore electrodes (radial component) and the other parallel to the electrodes (axial component). Each component can then be converted to a one-dimensional refractive index gradient with Eq. 2.

Because the measured refractive index gradient is directly related to the concentration gradients present in the system, it provides useful information about electrode reactions and mass transfer occurring within the model pore. The dependence of a refractive index gradient on concentration gradients is given by

$$\frac{\partial n}{\partial y} = \sum_i \frac{\partial n}{\partial c_i} \cdot \frac{\partial c_i}{\partial y} \qquad [3]$$

In the system used here, the two species of interest are potassium zincate and potassium hydroxide. The variation of refractive index with

concentration, $\frac{\partial n}{\partial c_i}(c_i)$, was measured for each of these[3]. The individual concentration gradients cannot, however, be determined so easily. Because the deflection data provide insufficient information to decouple the effects of two ionic species, it is necessary to compute the individual concentration gradients by a model and combine them according to Eq. 3. Only then can a meaningful comparison of theory and experiment be made. In Chapter III, a theoretical model of mass transfer in the model pore will be presented and checked against the experimental results set forth in this chapter.

B. Equipment & Methods

1. Detection System

A block diagram of the probe beam deflection system is shown in Fig.2. The detection system consists of the probe laser and a two-dimensional linear position detector. The probe beam source is a Uniphase 1103P 2-mW helium-neon laser with a $1/e^2$ beam diameter of 0.63 mm. The laser beam is focused into the model pore by a 52-mm focal length achromat lens. At the entrance and exit of the cell, the $1/e^2$ diameter of the beam is approximately 105 μm, and at the center of the cell it converges to a waist

---

[3] The technique employed to make these measurements and the results are discussed in Appendix I.

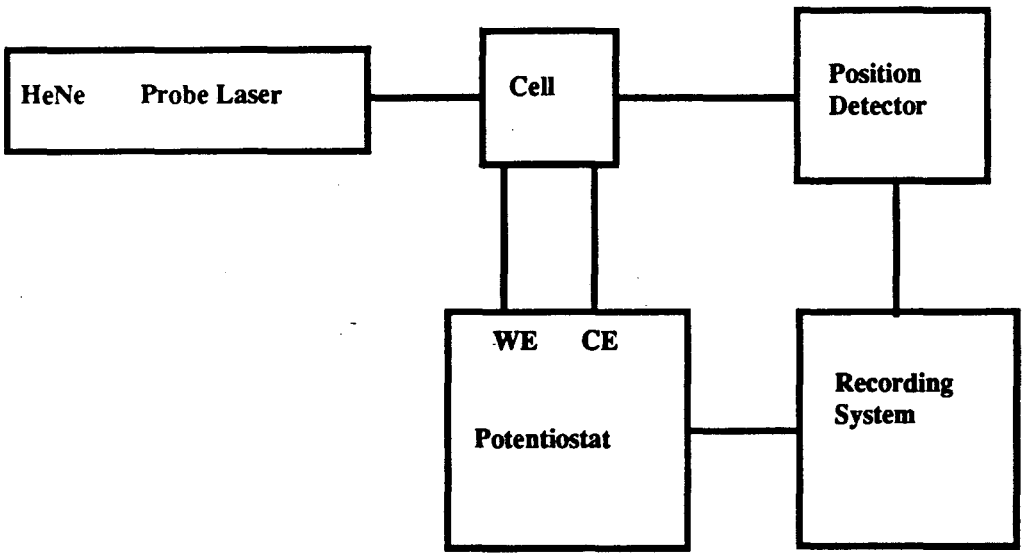

Figure 2. Schematic representation of the model pore cell and data-acquisition system.

diameter of approximately 75 μm. As the beam passes through the cell, along an axis parallel to the electrode, it is deflected by the refractive index gradient in the electrolyte. At the position detector, 20 cm from the cell, the deflection distance is measured and converted to a refractive index gradient as described above in Eq. 2. The linear position detector system consists of a United Detector Technology (UDT) SC-10D solid-state two-dimensional position detector connected to two UDT 301-DIV single-axis position monitors. The detector and associated position monitors produce voltage signals proportional to the distance that the beam has moved from the center of the detector face[4]. These signals result from local photocurrents generated in a planar semiconductor. All data are acquired by a Digital Equipment Corporation LSI-11/23 computer. These data include the cell current, voltage with respect to the Hg/HgO reference electrode, and the two components of beam deflection.

A number of environmental influences such as vibrations and air currents can degrade the quality of the beam deflection signal. Vibrations introduce noise which makes interpretation of small beam deflections

---

[4] More precisely, the position of the centroid of light intensity is monitored. This distinction becomes important if the concentration gradients are sharp enough to distort the shape of the beam as it passes through the electrolyte. This may be the case when the probe beam is positioned above the model pore mouth where the electrode meets an insulating surface.

difficult, whereas air currents (and their associated pressure gradients) cause gross displacements of the beam which may be interpreted as an actual signal. To reduce the influence of vibration, the entire system is mounted on a vibration-isolated 1.22m x 3.05m optical table (Newport Research Corp., Fountain Valley,CA). All instruments containing motors or other vibrating components, such as the potentiostat, are placed off the table. In addition, the cell, probe beam laser, and position detector are mounted on translation stages rigidly affixed to aluminum blocks which are in turn bolted to the optical table. Air currents are minimized by surrounding the entire detection system - the cell, laser and position detector - with insulating polystyrene foam slabs. In addition, the cell is surrounded by a smaller black posterboard box containing internal foam baffles.

2. Structure of the Cell

Schematic and perspective illustrations of the cell used in this study are provided in Fig. 3 and Fig 4 respectively. The electrolyte compartment is 1.5 cm long, 1.0 cm wide, and typically 200 μm high. This height (analogous to a cylindrical pore radius) was made large enough to allow the probe beam sufficient room to deflect in most experiments, while small enough to approximate real pore dimensions. The working and counter

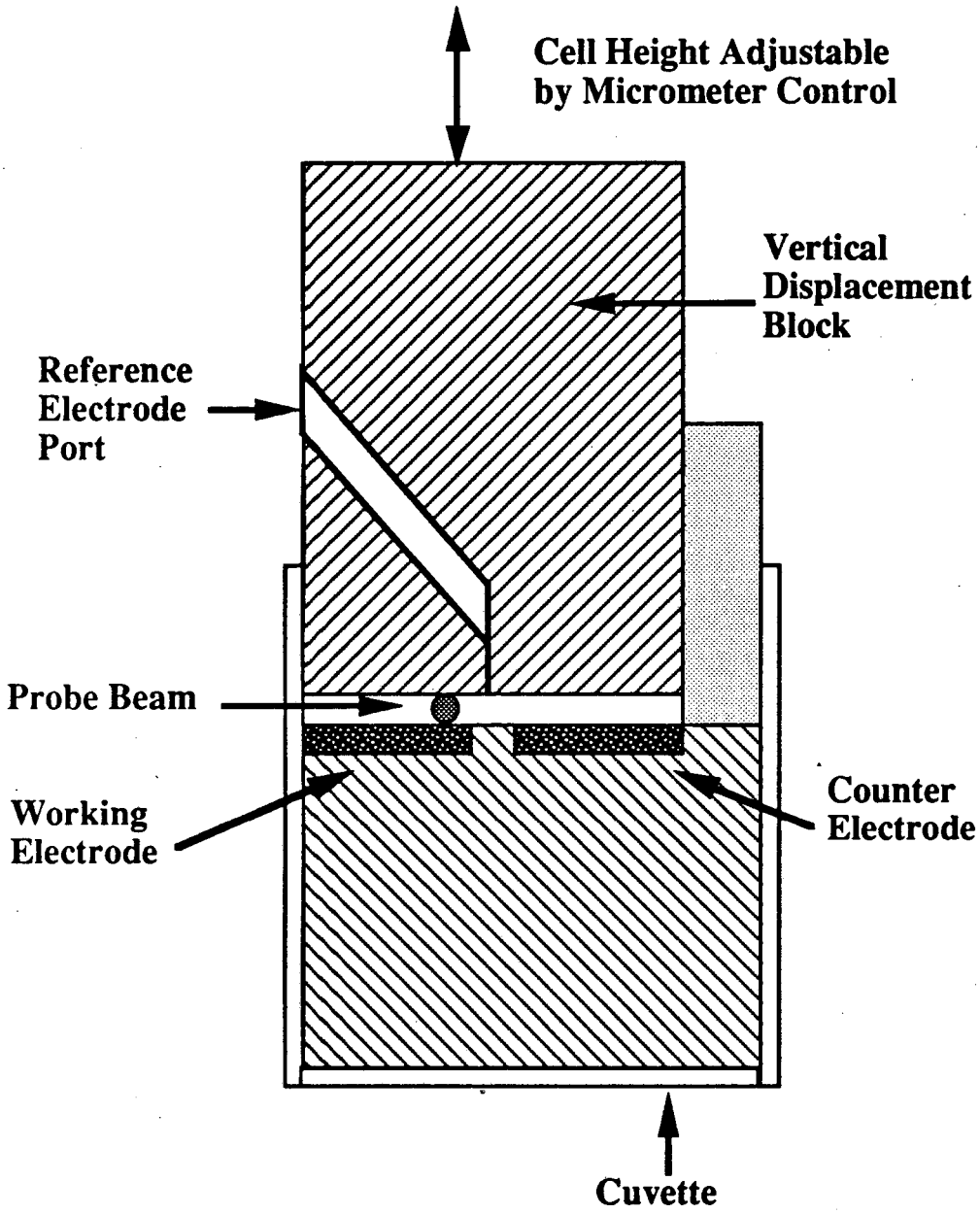

Figure 3. The vertical displacement block (acrylic) moves with respect to the other cell components so that the cell height (pore radius) can be accurately adjusted before each experiment.

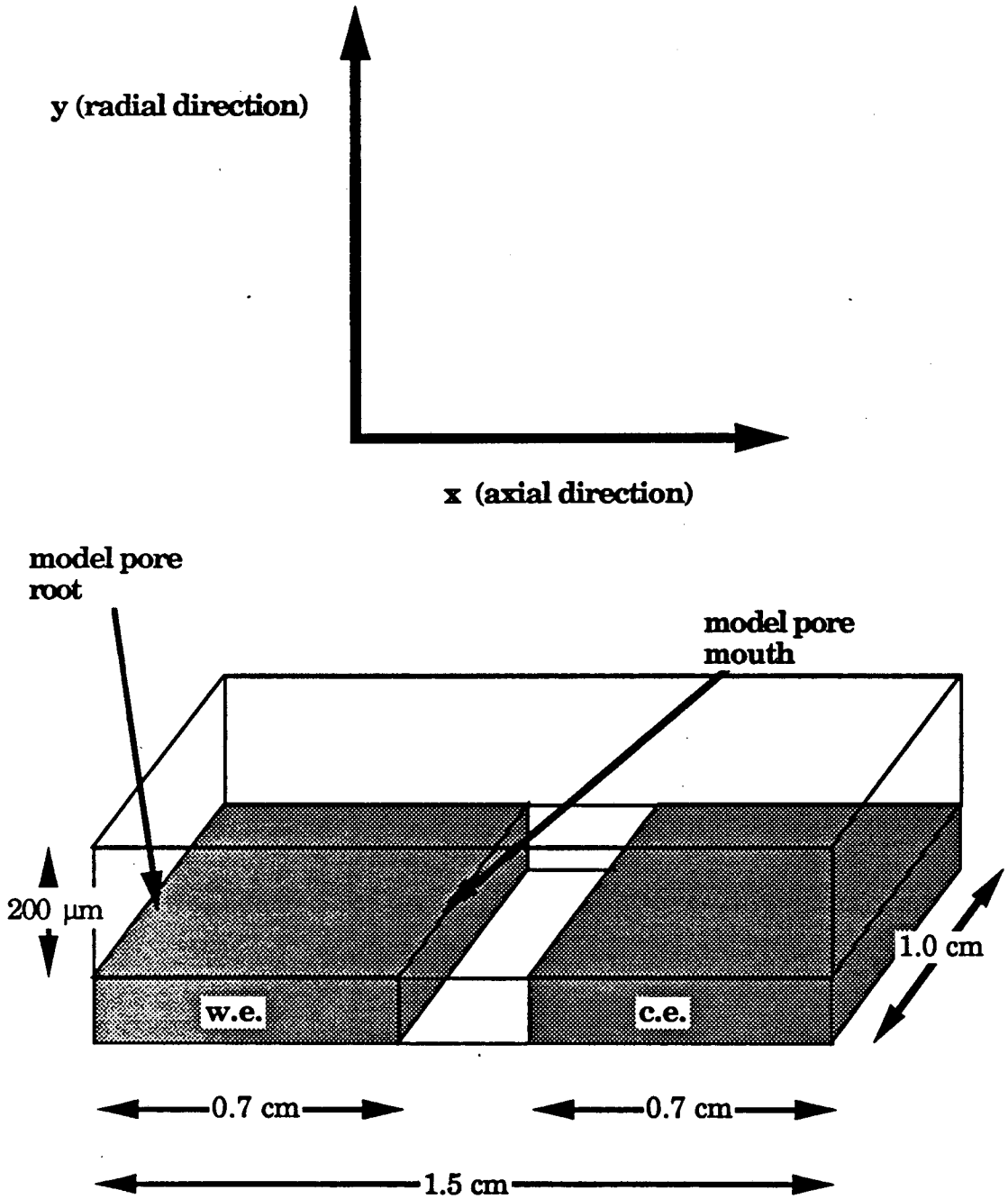

Figure 4. Perspective view of the model pore showing the axes used to describe the cell and typical dimensions of the model pore.

electrodes[5] at the base of the cell are each 1.0 cm wide by 0.7 cm long and are separated from one another by a 0.1 cm long strip of acrylic. The electrode length is sufficiently large to permit observation over a range of clearly defined axial positions within the cell. The region at the edge of the anode nearest the counter electrode is referred to as the pore "mouth", while the region at the opposite edge of the anode is referred to as the "root" of the model pore.

The two electrodes were mounted in a block of clear acrylic plastic with epoxy resin. The entire block was carefully machined to dimensions within a one-thousandth of an inch, so that it fit snugly in a 1-by-2-by-4 cm optical cuvette[6]. The cuvette formed the vertical walls of the cell and provided the entrance and exit windows for the probe beam. The upper boundary of the cell was defined by the polished bottom surface of another carefully machined block of acrylic. At the center of the upper cell boundary was a small hole (approximately 150 μm diameter) which served as an electrolyte conduit to a small Hg/HgO reference electrode and which also served as a port for introducing electrolyte into the cell. The upper block of acrylic (with the reference electrode) was mounted to a bracket

---

[5] The electrodes were cut from a 1-mm-thick sheet of 99.999% pure zinc (Aesar Co., Seabrook, NH).

[6] Uvonic Corporation, Plainview, NY.

which was, in turn, rigidly affixed to a translation stage[7]. This assembly permitted the top boundary of the electrolyte compartment to move independently of the rest of the cell with sub-micrometer precision. Thus, the cell height (analogous to the model pore radius) could be easily and accurately adjusted to investigate the effect of pore dimensions or to allow alignment of the beam before an experiment. Additional micrometer stages were attached to the aluminum block supporting the cell to permit translation in three directions, and rotation about the horizontal axis perpendicular to the probe beam. This arrangement facilitated alignment of the components along an optical axis.

Because we were investigating processes in a thin slot, the microstructure of the electrode surfaces was less important than the macroscopic flatness of the electrodes. With this in mind, the zinc electrode (plus acrylic) surface was prepared by two different techniques. In one, the electrode and acrylic face were ground on a flat glass surface with a succession of grinding powders, culminating with 9 μm alumina. Ultimately, the electrodes prepared by this technique developed a flat matte surface. In the second technique, the zinc/acrylic surface was machined with a high-speed cutting tool on a milling machine using alcohol as a lubricant. The resulting surface was reflective and unwarped. The deflection data obtained from these two types of electrodes were not

---

[7] This stage allows translation in one direction accurate to within 0.25 μm (Newport Research Corporation, Fountain Valley, CA).

noticeably different. However, the ground zinc electrodes were more likely to evolve gas bubbles during the course of an experiment. In order to suppress this reaction, the zinc electrodes were sometimes immersed in an alkaline 0.04 M $Pb(NO_3)_2$ solution[8] for approximately 30 s. If the electrodes were treated for much longer than this, the zinc would begin to corrode. The refractive index gradients measured with these lead-treated electrodes were indistinguishable from those of the untreated electrodes.

3. Description of Experiments

All experiments described here were conducted galvanostatically, using total cell currents of 0.25 mA, 0.50 mA, or 2.22 mA. These currents correspond, roughly, to slow, normal, and rapid discharge of a secondary alkaline zinc/nickel oxide cell. Table 1 provides comparisons between the model pore (assuming 0.5 mA total cell current) and a typical porous electrode for a variety of current density definitions. The *typical electrode* chosen for comparison is the negative electrode of a 1.35 Ah zinc/nickel oxide cell discharged at 0.5 A (13). It has a facial area of 43.4 cm^2, a thickness of 0.1 cm, and a porosity of 0.75. In this cell, the negative zinc electrode is sandwiched between two nickel oxide electrodes. Thus, each face of the zinc electrode sees only one-half of the total current. To calculate

---

[8] Lead-containing additives are commonly added to zinc electrodes to suppress hydrogen evolution (11,12).

Table 1

Comparison of current densities for a model pore and a typical porous electrode

Area or volume basis	Electrode Face (mA/cm^2)	Pore Mouth (mA/cm^2)	Pore Wall (mA/cm^2)	Electrolyte Vol. (mA/cm^3)
Typical Porous Electrode	5.8	7.7	0.19	154.
Model Pore	18.8	25	0.714	35.7

the surface area of a single pore in such an electrode, each macropore is assumed to be a cylinder of diameter 50 μm and length 0.05 cm.

As Table 1 shows, values for the model pore and typical porous electrode agree to within an order of magnitude for each definition of current density. Since the model pore is an abstraction of a real pore, with a quite different geometry, good agreement cannot be expected for every definition of current density. Rather than designing a system that agreed exactly with one definition of current density, we chose a cell size and current that permitted reasonable comparison between abstraction and reality for several definitions of current density.

The electrolyte used in this study was prepared from 15 or 31 wt% aqueous potassium hydroxide solutions saturated with zinc oxide. To ensure complete saturation, the solutions were stirred for at least three days in the presence of excess zinc oxide. Afterward, they were periodically purged with argon gas to prevent conversion of hydroxide to carbonate ions as a result of air ingress. After the cell height was adjusted, electrolyte was introduced via a syringe into the model pore through the reference electrode port, and the cell was aligned with respect to the probe beam. Before each experiment, the probe beam position was recorded for 45 s before the current was applied, to determine whether it was drifting in the absence of electrochemical reactions. Current was then passed for approximately 1000 s before the system was returned to open circuit and the gradients were allowed to decay. The response of the system was then usually recorded for at least an additional 150 s. After each experiment, the

electrolyte compartment was examined for the presence of bubbles or precipitate. The electrode surface was then ground or machined and washed in preparation for another experiment.

To gain insight into how concentration gradients and current distribution vary along the axial direction of a pore, experiments were performed at different probe beam locations. In the model pore, four different evenly-spaced positions were chosen. Thus, four sets of experiments were conducted for each system: one in which the probe beam was positioned at the electrode mouth (the position nearest the counter electrode) and three others at different positions, equally spaced toward the pore root. Positioning the cell for each new experiment was easily achieved by translating the electrode position horizontally, perpendicular to the probe beam axis.

To ensure that the beam position for these different experiments along the pore axis was consistent, a technique for finding the edge of the electrode was developed. In this method, the cell is moved vertically until the probe beam is blocked by the edge of one zinc electrode. Next, the cell is translated horizontally until the probe beam passes freely between the working and counter electrodes (in this region it can pass through the relatively transparent acrylic since it is no longer blocked by the zinc). Finally, the beam is moved horizontally across the edge of the zinc electrode so that the distance between where the beam becomes completely visible and where it becomes completely obscured can be determined. The position

halfway between these two extremes is designated as the pore mouth, at XR=1.00 on a dimensionless coordinate axis.

C. Results

Figure 5 shows typical refractive index gradient profiles in the direction normal to the electrode. For these experiments (and for most others), the normal component of refractive index gradient grew rapidly for 20 to 50 s before leveling off to a relatively constant magnitude. In some instances, this leveling did not result in the gradient remaining completely constant, rather it would grow or decline slightly with time. But in all instances, the deflection profile in this regime remained markedly constant in comparison with the initial rapid growth. We also observed that the absolute magnitude of these gradients depended strongly upon the vertical position of the probe beam. Figure 6 shows this effect for a series of 0.25 mA experiments, each lasting 100 s. As expected, the magnitude of deflection becomes larger as the beam is moved closer to the electrode. Thus, accurate and reproducible vertical positioning of the beam is important. To accomplish this, the probe beam was centered by compressing the cell height (the distance between the electrodes and the top of the cell) until a shadow of the cell appeared on the beam image. Then the position of the cell relative to the beam was adjusted to remove the shadow. This procedure was repeated until the cell height could not be reduced without producing a shadow. Finally, the model pore was reopened to the height used in the experiment, and the beam was recentered in the cell by moving the cell one-half the distance required to reopen the pore.

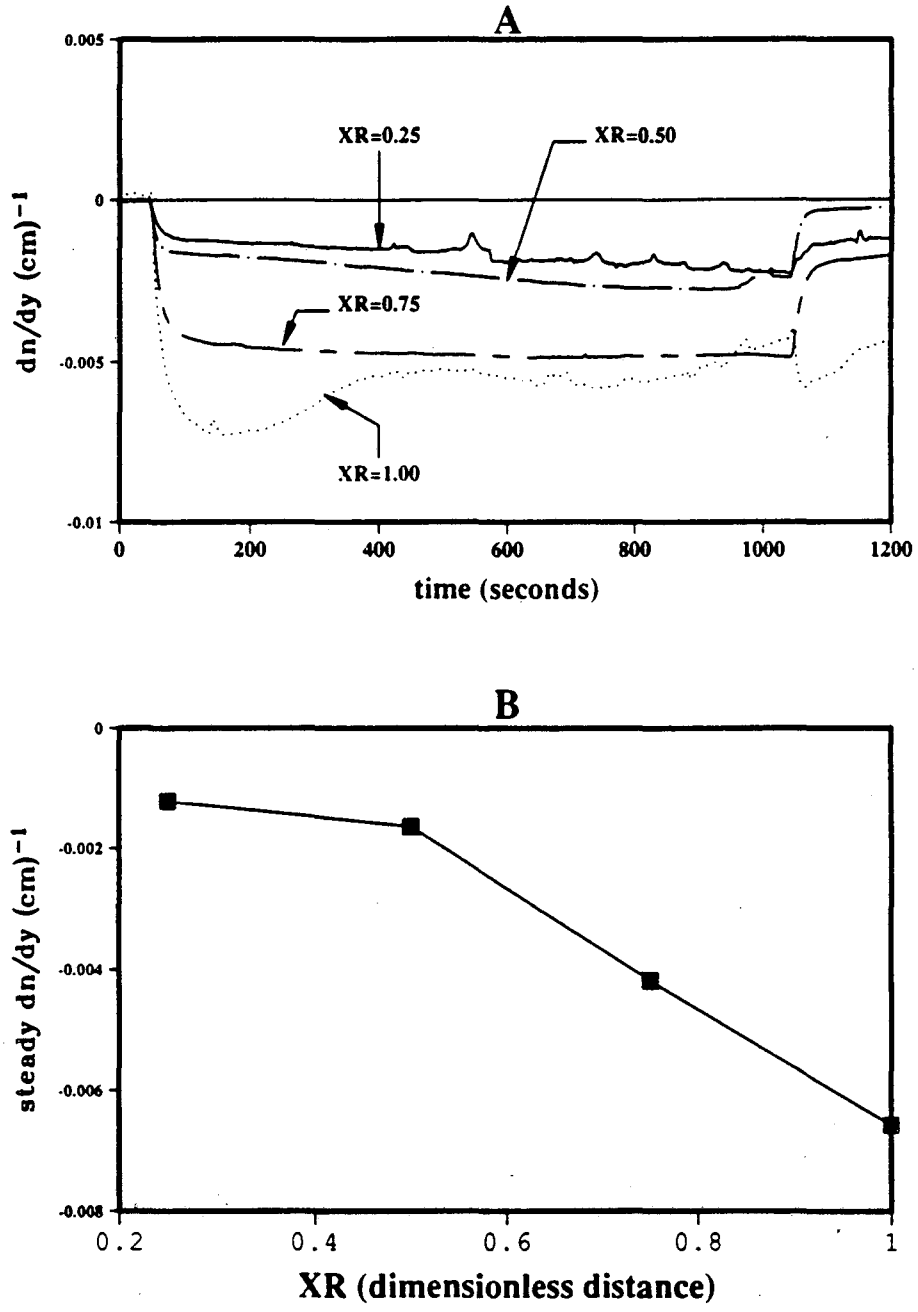

Figure 5. Refractive index gradients normal to the plane of the model pore anode as a function of time. Typical results for 31wt% KOH saturated with $K_2Zn(OH)_4$ electrolyte and 0.5 mA total current are shown in A for four locations within the model pore. The dimensionless distance is measured from XR=0 at the model pore root to XR=1 at the model pore mouth. The size of the gradient at the shoulders of the curves shown in A (55 s after current begins passing) are presented together for the four probe beam locations in B.

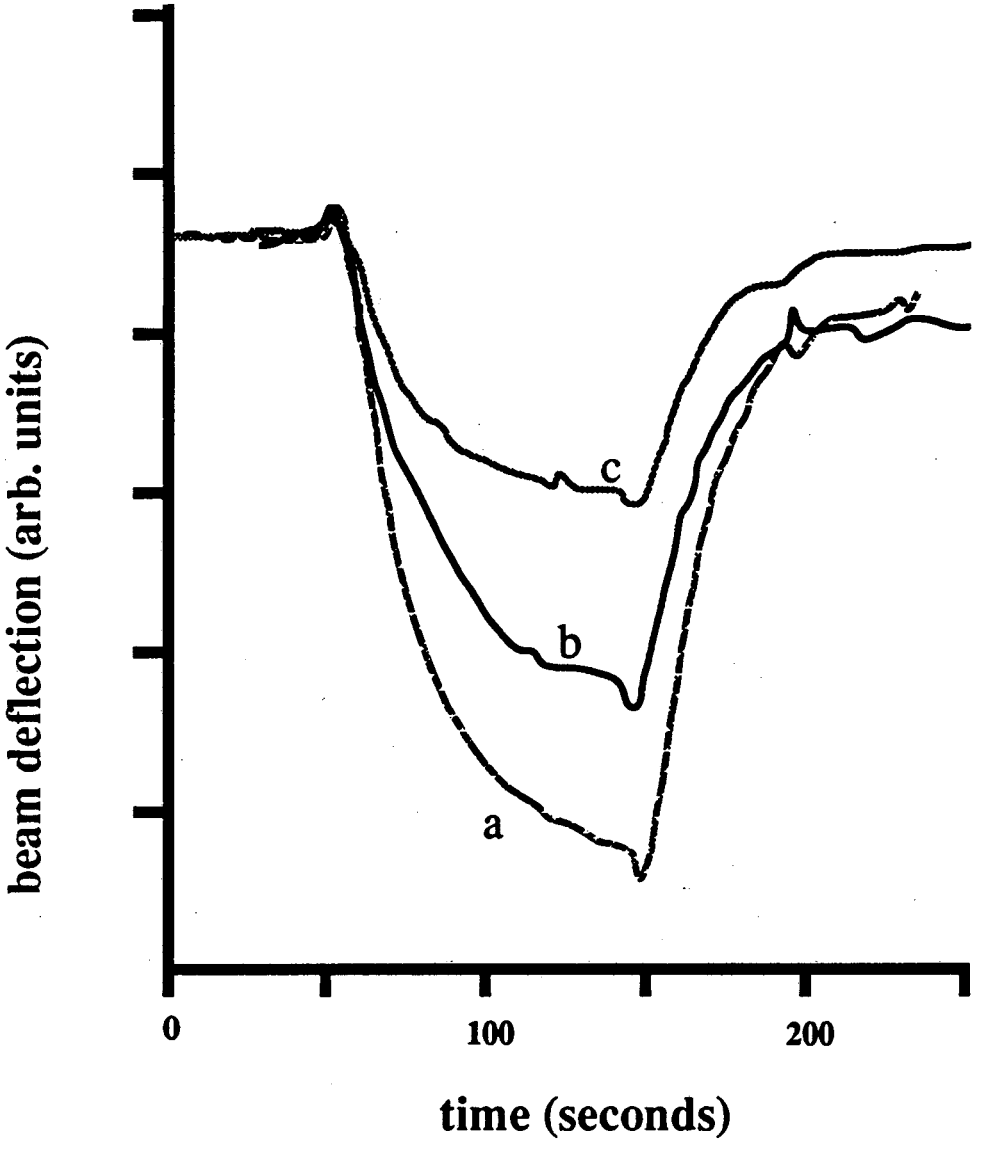

Figure 6. The effect of beam distance from the anode on the beam deflection for short current steps. For curve b, the beam was centered in the electrolyte compartment (approximately 100 μm above the anode surface) according to the procedure described in the text. For curve c, the beam was moved 20μm farther away from the anode. Finally for curve a, the beam was positioned 20μm closer to the anode than it was in curve b. In each case 0.25 mA of current was passed through the cell for 100 s.

All values of the gradients shown in Fig. 5 are negative, indicating that the beam was deflected toward the electrode. In terms of solution properties, this means that the refractive index was greater near the electrode. The significance of this and other observations will be discussed quantitatively by comparison to a two-dimensional model in Chapter III. However, the qualitative physical significance of negative deflections can be understood in terms of the solution properties of the soluble species and the reaction stoichiometry at the zinc electrode. The electrochemical reaction at the zinc anode is

$$Zn + 4OH^- = Zn(OH)_4^{-2} + 2e^- \qquad [4]$$

The proportionality between the rate of generation of zincate ions and the consumption rate of hydroxide ions means that the concentration gradients of these two species at the electrode will grow simultaneously but in opposite directions. According to Eq. 3, the solution refractive index gradient grows or decays in response to changes in these concentration gradients. Since $\frac{\partial n}{\partial c_i}$ is positive for both species (see Appendix I) and the two concentration gradients grow in opposite directions, the two terms in Eq. 3 must have opposite signs. By deflecting toward the anode, the beam is thus responding primarily to the zincate concentration gradient. In other words, the zincate term is the larger of the two terms in Eq. 3. This is not surprising because the diffusion coefficient of zincate is smaller than that of potassium hydroxide, and the magnitude of $\frac{\partial n}{\partial c_i}$ is greater for potassium zincate.

It can be seen from Fig. 5 that the normal component of the refractive index gradient attained its largest magnitude near the model pore mouth and decreased steadily toward the root. This suggests that the normal component of the zincate concentration gradient was largest near the pore mouth. These observations can provide some insight into the current distribution within the model pore. If Faraday's law and Fick's law of time-independent diffusion are assumed to apply (i.e. the transfer current density is proportional to the concentration gradient of the solute), then it is reasonable to assume that the progression of beam deflections along the pore length approximately reflects the transfer current density distribution within the model pore. Hence, we expect that the transfer current density decreases when moving from the pore mouth to the pore root.

Figure 7 presents the axial component of beam deflection for three positions along the model pore's axis[9]. The quantitative aspects of these gradients will also be discussed in Chapter III, but three qualitative observations are immediately apparent. First, the direction of the gradient changes from negative to positive between the mouth of the model pore (dimensionless distance XR=1.00) and XR=0.75 and remains positive for

---

[9] The gradients at XR=1.00 were so large that they would typically cause the laser beam to deflect beyond the edge of the position detector. This resulted in the flat section on the curve shown in Fig. 6.

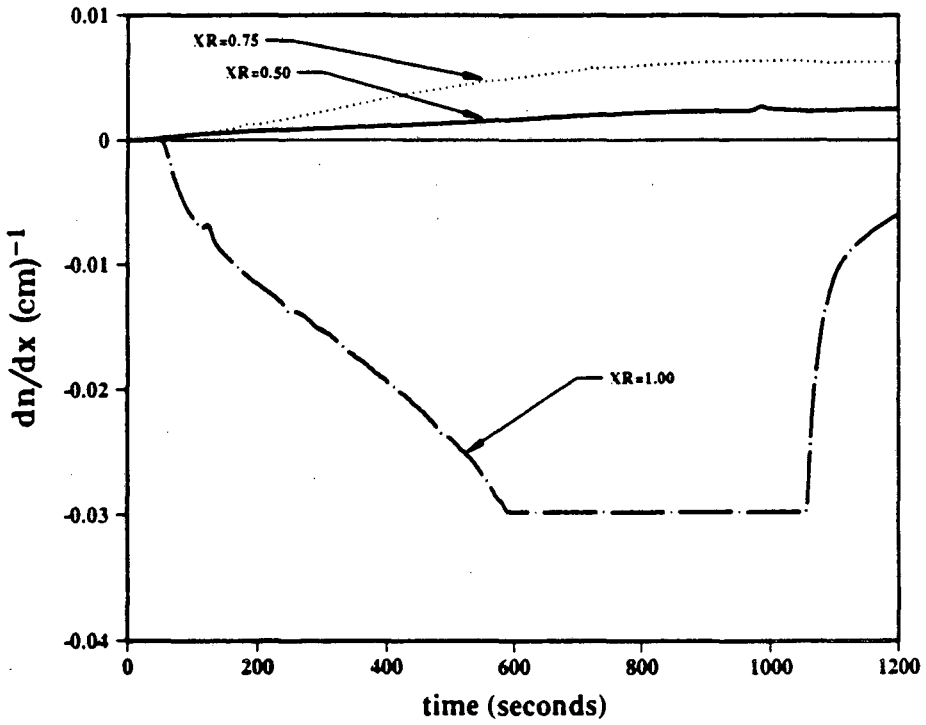

Figure 7. Refractive index gradients in the axial direction of the model pore. These results correspond to those shown in Fig. 5 (31 wt % KOH saturated with $K_2Zn(OH)_4$ electrolyte and 0.5 mA total current) for three positions within the model pore above the anode.

smaller values of XR. Second, the gradient becomes smaller in magnitude as the beam position is moved from XR=0.75 toward the root of the pore. Finally, it should be noted that these gradients grow more slowly than their counterparts in the direction normal to the model pore electrode[10]. From these observations, at least one preliminary conclusion can be drawn. As noted earlier, the direction of the refractive index and the zincate concentration gradients are expected to coincide. Thus at the mouth of the pore, the negative value of the axial beam deflection indicates that the zincate concentration gradient is negative (the zincate concentration decreases toward the counter electrode). Likewise, the positive value of deflection at XR=0.75, indicates that the concentration gradient of zincate corresponds to an increasing concentration toward the mouth of the pore. Presumably then, the axial zincate concentration distribution reaches a maximum between XR =1.00 and XR = 0.75.

It should be noted that at long times (> 500 s.), both components of deflection often became noisy, losing their smooth profiles. This may have been due to bubbles which in some instances were observed forming in the electrolyte compartment. It is, of course, also possible that sustained

---

[10] In most instances, these gradients grew steadily as shown in Fig. 6. In a few other instances, however, the beam deflection reached a maximum and then began to decrease in magnitude before the cell current returned to zero. We believe that convection resulting from density gradients probably caused this effect.

density gradients associated with the concentration profiles in the model pore drove natural convection which disrupted the steady beam deflection. If convection was present in the cell, it should have been most prominent near the pore mouth where the concentration differences were greatest. This is indeed what was observed. Signals at the model pore mouth (XR=1.00) showed the most variation between different runs and also showed the most fluctuation during the course of a single experiment.

To better assess the model pore behavior under a range of conditions expected in an actual porous electrode, additional experiments were conducted in which the electrode polarity, the cell current, and the electrolyte concentration were each varied. Figure 8 shows the typical effect of electrode polarity on the gradients normal to the electrode. In the particular experiment shown here, the cathodic-polarity experiment was conducted in the same cell and electrolyte as the anodic-polarity experiment. Note that, as might be expected, the gradients moved in opposite directions and had roughly equal magnitudes at short times. However, at longer times the cathodic-polarity deflection gradually decreased from the steady value apparently achieved earlier in the experiment. This may have been a result of the hydrodynamic instability of the solution over the cathode, where the more concentrated (and thus heavier) zincate solution near the top of the cell probably began to flow downward.

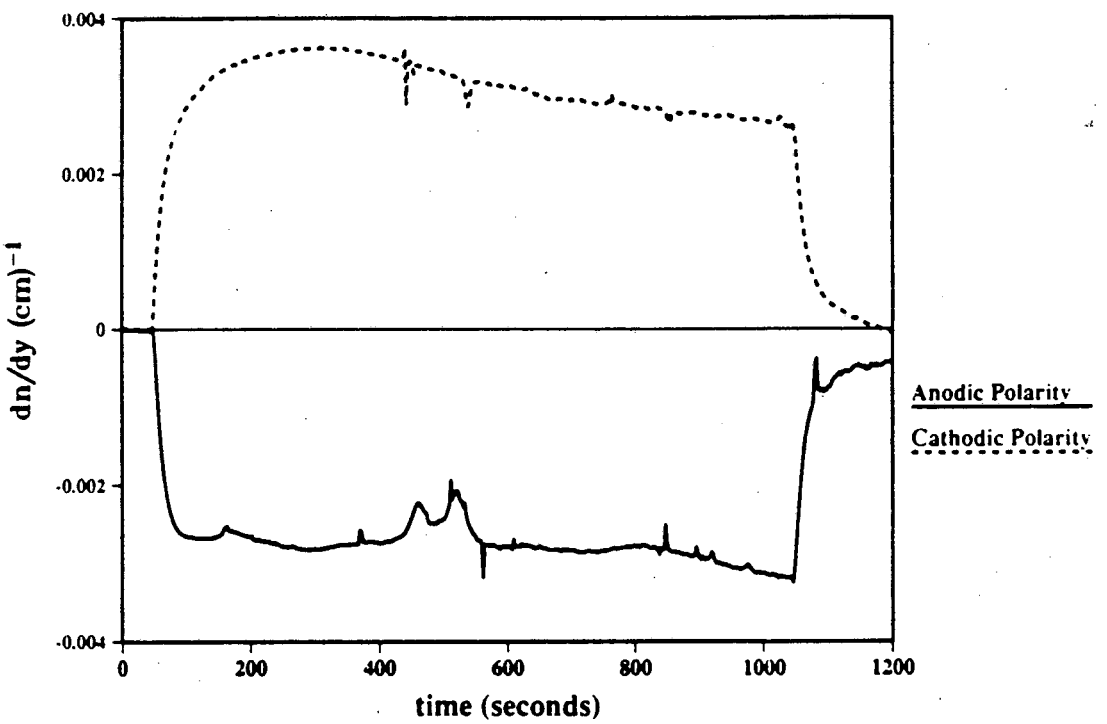

Figure 8. The effect of current polarity on refractive index gradient in the radial direction (normal to the plane of the electrode surface) for experiments employing 31wt% KOH saturated with $K_2Zn(OH)_4$ electrolyte and 0.5 mA total cell current. The beam was positioned at XR=0.50.

Because a battery may be discharged at various rates, it is important to compare the results obtained for different total cell currents. Figure 9 shows how the axial components of the refractive index gradients decreased in magnitude when the cell current was decreased from 0.5 mA to 0.25 mA. This can be understood in terms of Faraday's law which predicts that the zincate ion flux along the electrode should diminish with lower currents. Likewise the size of the flux should increase at higher currents. Unfortunately, at relatively high currents (2.2mA), bubbles often formed and interfered with the beam, making investigation with probe beam deflection impossible. Nevertheless, some deflection data for higher current densities were obtained for short times and will be discussed in Chapter III.

The deflection results for experiments conducted with 15 wt % (rather than the 31 wt% used so far) potassium hydroxide saturated with zinc oxide are shown in Fig. 10. These results are of interest because other investigators have suggested that zinc electrode shape change might be minimized by lowering the concentration of potassium hydroxide, and thereby lowering the concentration of soluble zinc species as well (12). Comparison of Fig. 10 with Fig. 5 shows that the results from low concentration electrolyte experiments follow the same general beam position dependence as those obtained from experiments with 31 wt % potassium hydroxide saturated with zinc oxide. The magnitudes of these gradients are also comparable to those observed in the higher-concentration electrolytes. Thus, we may expect that the zincate and hydroxide ions will

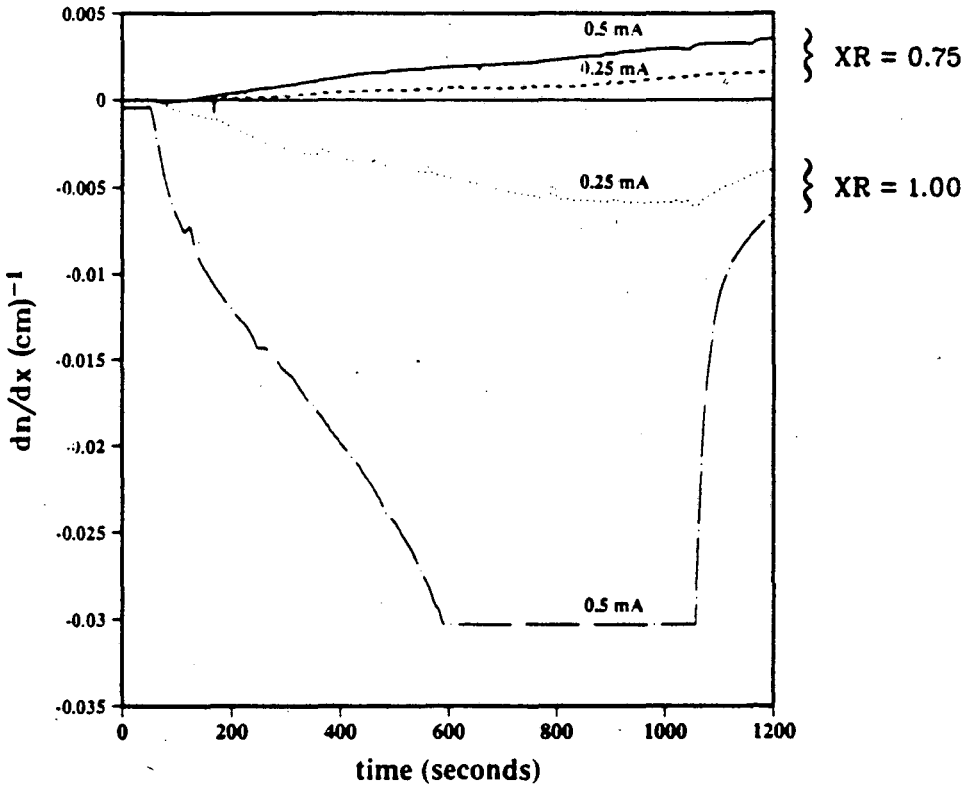

Figure 9. The effect of current variation on refractive index gradients in the axial direction (parallel to the plane of the anode surface) for experiments employing 31wt% KOH saturated with $K_2Zn(OH)_4$ electrolyte and 0.5 mA total cell current.

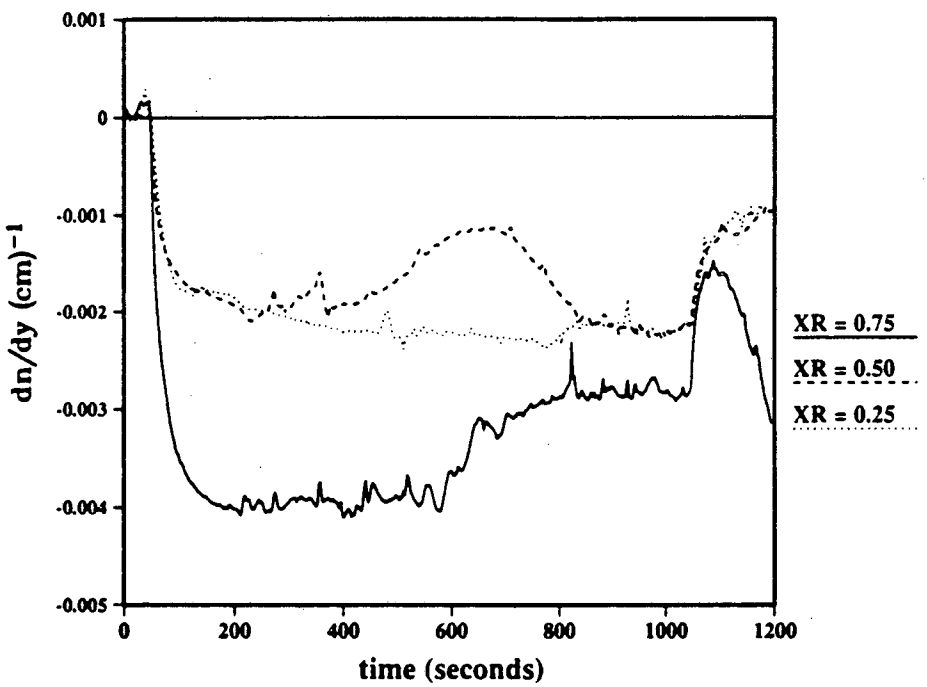

Figure 10. Refractive index gradients in the radial direction for anodic experiments conducted in 15wt% KOH electrolyte saturated with ZnO at 0.5 mA total cell current.

be driven by diffusion at comparable rates in 31 wt% and 15 wt% electrolytes.

We considered the possibility that temperature gradients within the electrolyte might contribute to the observed beam deflection. This would occur, for instance, if the electrolyte absorbed some radiation from the probe beam and generated a temperature gradient which might be detected as a refractive index gradient. To test this possibility, we conducted a series of runs in which the probe beam power was reduced by 50% with a neutral density filter. The results of these runs were indistinguishable from those conducted without a filter. Other possible sources of temperature gradients are Joule heating in the electrolyte and the heat of reaction at the electrodes. Both of these factors can, however, be shown to have a negligible effect on the refractive index of the electrolyte. Thus, we assumed that temperature effects had little effect on the deflection measurements.

Reflection from the upper or lower surface of the cell is another possible source of interference. Since the probe beam shape is gaussian, its intensity distribution will, in theory, extend infinitely in the direction normal to propagation. Thus, there will always be some reflection. However, for practical calculations the beam radius is taken as the distance from the beam centerline to a point where the intensity reaches $1/e^2$ of its maximum. For the model pore, this means that the edge of the beam

begins to be reflected if it is deflected by 45 μm[11], corresponding to a gradient of 0.0045 cm^{-1}. This value was derived by assuming (conservatively) that all the deflection occurs abruptly at the beam entrance rather than gradually over the width of the electrode as it does in practice. Thus 0.0045 cm^{-1} might be considered the minimum refractive index gradient for which reflection contributes to the signal. As the beam is deflected further, reflection increases following a gaussian distribution until the beam centerline strikes the electrode. This could occur for a gradient of 0.010 cm^{-1}. Although this value is based upon an exaggerated estimate of beam deflection and is therefore very conservative, it does coincide with the largest gradient values actually measured[12]. Thus, for the component of deflection normal to the electrode, reflection cannot be ruled out as a contributing factor, especially where larger gradients are encountered.

---

[11] This assumes a rather large beam diameter of 110 μm. For the 52 mm focal length lens used with our HeNe laser, the beam should focus to approximately 75 μm in the center of the model pore and diverge to approximately 105 μm at the entrance and exit.

[12] In the experiments we conducted, the maximum recorded gradient normal to the electrode surface was approximately 0.011 cm^{-1} for a cell current of 0.5 mA, and 0.012 cm^{-1} for a cell current of 2.2 mA. For measurements where much larger deflections were expected (e.g. at the model pore mouth during 2.2 mA experiments), the beam deflection often became unstable or reversed direction abruptly.

Precipitation within the electrolyte is another physical process that might affect the observed probe beam deflection. Katan *et al.* (3) observed a flocculating precipitate at volumetric current densities of 1.2 to 4.8 A/cm^3. This was presumably the type I precipitate described by Powers *et al.* (14). This is in accord with the observation that actual porous zinc electrodes from galvanic cells are converted to zinc oxide during discharge (15). Since there is often no evidence of passivation accompanying this reaction, most of the zinc oxide is probably formed as type I precipitate. To determine when precipitation should be expected in the optical probe beam deflection experiments, a model pore cell suitable for observation with optical microscopy was constructed. Flocculating precipitate was observed at current densities approaching those employed by Katan *et al.* However, at current densities near those used in the optical probe beam deflection experiments (and closer to those expected in a zinc/nickel oxide cell), no precipitation was observed. If precipitation was to occur in the model pore during deflection experiments, it would be immediately noticeable in the detection system. Precipitation would cause an abrupt change in deflection (the reaction stoichiometry and the hydroxide and zincate formation rates would change rapidly). Additionally, the beam would be scattered by the small precipitate particles resulting in an abrupt decrease in the total current generated on the position detector. We observed no precipitate in the electrolyte[13]. This is probably because the electrolyte concentration of

---

[13]As noted above, the zincate concentration reaches a maximum between XR=1.00 and XR=0.75. Even in this region, no precipitation was observed.

zincate could not reach a sufficiently high level of supersaturation to permit rapid precipitation. Because the zinc positive electrode in the model pore consumes zincate ions, the expected zincate concentration should be somewhat smaller than that encountered in actual secondary batteries. Most common positive electrodes used with zinc in secondary cells (e.g. NiOOH, AgO or air electrodes) do not consume large amounts of zincate ion and therefore allow higher concentrations of zincate ion to build up which enhances the likelihood that the type I precipitate will form.

D. Summary & Conclusions

A new optical probe beam deflection system was developed to study the processes occurring within a single pore of an alkaline zinc electrode. We have shown that probe beam deflection can be usefully applied to characterize mass transfer processes within a model pore cell designed to simulate a single electrode pore. The system can monitor refractive index gradients in two dimensions within the model pore. These refractive index gradients reflect contributions from the potassium hydroxide and potassium zincate concentration gradients present in the electrolyte. The measured components of the refractive index gradients were a strong function of the total cell current and the position along the model pore axis. Other factors influencing the beam deflection included the cell polarity, the vertical beam position, and the electrolyte concentration.

Chapter III Theoretical Analysis and Discussion

A. Motivation for the Numerical Model

This chapter presents a theoretical framework and associated numerical model for interpreting the probe beam deflection results set forth in Chapter II. Because the refractive index gradients that are measured by probe beam deflection represent a sum of the contributions caused by the concentration gradients of each electrolyte specie, a model is necessary to separate the individual contributions. The model described here allows direct calculation of the local concentration and current distributions within the model pore electrolyte. Consequently, the concentration gradients, and ultimately the probe beam deflection, can be calculated for any point in the model pore. These results, taken together with the experimental results, help to describe the physico-chemical events occurring within a single pore, and may ultimately suggest conditions that will promote better utilization of the electrode active materials, and improved electrode performance and lifetime.

Relatively few investigators have combined numerical modeling and experimental studies of a single pore within a porous electrode. However, several authors have developed independent single-pore theories of varying degrees of sophistication. De Levie reviewed the earliest attempts to derive analytic solutions describing the behavior of single pores (16). These attempts usually did not account for mass transfer, or treated it as a steady-state phenomenon. Typically, linear charge transfer kinetics were used,

although in some instances Tafel kinetics were employed. More recently, numerical techniques have allowed more realistic physical descriptions, which often include transient mass transfer, potential distributions and nonlinear kinetics within a single pore (17,18).

In parallel with the above work, a macroscopic view of the entire porous electrode was developed. In this view, the porous electrode is treated as a superposition of two continua: the electrolyte phase and the electrode matrix phase. The development and application of this approach was reviewed by Newman and Tiedemann (19). Since then, numerous investigators have applied the macroscopic view to model a variety of porous electrode systems in one dimension[14], including the alkaline zinc electrode (18,20). One advantage of this approach is the ease with which it may be applied to complex systems. Since it treats the porous electrode as a continuum, the equations to be solved are identical to those used in non-porous media, e.g. the equation of convective diffusion in a homogeneous solution. However, the parameters used in such models have different physical interpretations from their counterparts in single-phase problems. The macroscopic parameters are volume-averaged quantities which

---

[14] Isaacson et al. (22) have developed a two-dimensional model of the porous zinc/zinc oxide electrode based upon the macroscopic continuum view of porous electrodes.

depend upon the porosity, tortuosity, or other detailed characteristics of the porous structure[15] (22,23).

As de Levie has pointed out, the equations for continuum models are analogous to those for a single pore (16). However, the macroscopic approach cannot be expected to depict events within a single pore accurately. For instance, the variety of pore sizes and shapes should cause the concentration to vary between neighboring pores and even within a single pore. Such localized changes in concentration will lead to local variation in the values of concentration-dependent parameters such as the exchange current density, and might thereby drive some reactions much faster or slower than anticipated. This could lead to processes of a far different character than accounted for in a corresponding macroscopic model (e.g. zinc oxide may precipitate within some pores of a porous electrode but not others). Thus, a study of single pores, independent of the entire electrode, is necessary.

Dunning *et al.* (17) developed a numerical model of mass transfer within a single cylindrical pore. The major focus of their work was the growth and coverage by a sparingly-soluble salt film on a cylindrical pore wall in $Cd/Cd(OH)_2$ and Ag/AgCl electrodes. Their model incorporated

---

[15] Recently, approaches such as those based upon fractal geometry have also been employed to calculate average-value quantities (21).

concentration-dependent electrolyte properties and allowed soluble salts to complex with the bulk electrolyte anion. In addition, the pore radius and charge transfer resistance were permitted to change during the electrochemical reaction due to salt precipitation. Although their treatment incorporated many important features of a single pore, it was limited to one dimension and a cylindrical geometry. Liu *et al.* (18) and Yamazaki *et al.* (24) have developed models to explain experimental results obtained with an array of microscopic cylindrical pores in a segmented zinc matrix. Although their experimental approach was based on a series of single microscopic pores, the information it provided was macroscopic in nature, limited to the matrix current of each zinc segment. Thus, the numerical models used to describe their results were grounded in the macroscopic theory of porous electrodes. Like the Dunning *et al.* model, these models were one-dimensional and based upon a cylindrical pore geometry.

As the above examples suggest, the pertinent pore models have been almost exclusively one-dimensional. The direction modeled usually corresponds to what we refer to as the axial component of the model pore, i.e. the direction normal to the face of the macroscopic porous electrode. In some instances this one-dimensional approach will be justified,[16] in

---

[16] This may occur, for example, when the penetration depth (i.e. the square root of the ratio of the charge transfer resistance to the ohmic resistance) is greater than the pore diameter (16).

particular when only the current density distribution is of interest. In these probe beam deflection studies, however, it becomes important to consider a second dimension: the radial direction (normal to the plane of the electrode in the model pore). The refractive index gradients in this direction provide valuable insight into the transfer current density distribution within the model pore. Also, the model must account for the observed strong dependence of the refractive index gradients on distance in the radial direction.

A few two-dimensional models from outside the porous electrode literature have applied to geometries similar to that of the model pore. However, none of these completely describes the model pore cell, shown in Fig. 11. For example, Hume *et al.* (25) developed a model of steady-state mass transport to a planar cathode in a photolithography system. The geometry they considered resembled the cathodic half of the model pore, but the bottom insulating surface was raised slightly above the plane of the cathode. In addition, some of the non-electrode boundaries were not treated as insulators and charge transfer resistance was not considered. Morris and Smyrl (26) have developed a model of the potential distribution - without including mass transfer - for a thin rectangular galvanic cell very similar to the model pore. On the bottom of their cell, an anode and coplanar cathode abutted one another. The remaining three sides of the domain were insulators. Thus, the boundaries of this cell were identical with those of the model pore, except that there was no thin insulating strip between the anode and cathode

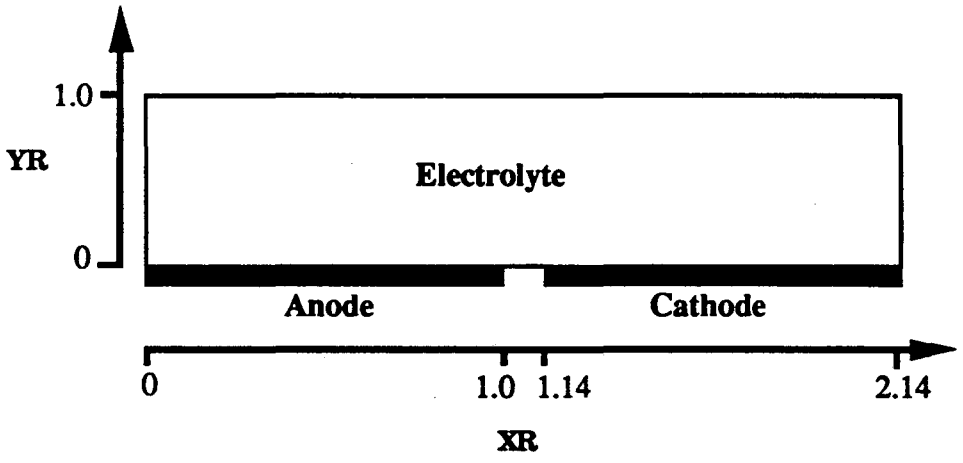

Figure 11. Diagram of the model pore cell geometry. XR is the dimensionless distance in the direction parallel to the electrode surface. YR is the dimensionless distance in the direction normal to the electrode surface.

B. Development of the Single-Pore Model

1. The Zinc Electrode

The first step in the discharge of a porous zinc electrode is the electrochemical dissolution of zinc to form the zincate ion

$$Zn + 4OH^- = Zn(OH)_4^{2-} + 2e^- \qquad [4]$$

This dissolution reaction proceeds along with a subsequent precipitation reaction in which zinc oxide is formed. A combination of these two sequential reactions then gives the overall anodic reaction of the alkaline zinc electrode

$$Zn + 2OH^- = ZnO + H_2O + 2e^- \qquad [5]$$

Two types of electrochemically formed zinc oxide have been observed (14). The first type is a loose porous film that apparently originates in the electrolyte phase. The second type is a compact, tightly adherent film that may form directly on the electrode surface, and is accompanied by electrode passivation. In these experiments, the current density was maintained at sufficiently low values to study the dissolution reaction independently, uncomplicated by either form of precipitation. Thus, this description of the model pore focuses solely on the dissolution reaction, Eq. [4].

2. Mass Transfer

In order to simplify treatment of the model pore geometry in two dimensions, we eliminated the potential terms where possible and employed the basic tenets of dilute solution theory. However, the values of the parameters used in the numerical model are appropriate for the higher concentrations present in the alkaline zinc electrode. The material balance is solved for both potassium hydroxide and potassium zincate in the domain of the model pore

$$\frac{\partial c_i}{\partial t} = -\nabla \cdot N_i + R_i \,. \qquad [6]$$

Here N_i is the flux of species i in solution and R_i is the rate of reaction per unit volume in the electrolyte. If there is no convective mass transport within the model pore[17], the solute flux includes contributions from diffusion and migration only. If, in addition, the diffusion coefficient is invariant with concentration and there are no homogeneous reactions, Eq. [6] can be recast as follows:

$$\frac{\partial c_i}{\partial t} = D\,\nabla^2 c_i + \frac{z_i F D}{RT}\,\nabla \cdot (c_i \nabla \Phi) \qquad [7]$$

---

[17] Because of the high flow resistance within a flooded porous electrode, the electrolyte is expected to be relatively quiescent in the absence of forced convection (15,16).

where z_i is the charge associated with each ion and Φ is the potential within the solution. As written, Eq. [7] applies separately to each ionic species present. For binary electrolytes, the expressions for each of the two ionic species can be combined to eliminate the potential term giving the equation of time-dependent diffusion

$$\frac{\partial c_i}{\partial t} = D_{eff} \nabla^2 c_i \qquad [8]$$

where D_{eff} is the effective diffusion coefficient for the neutral combination of ionic species.

In solutions containing a supporting electrolyte together with a minor component, Levich (27) suggested treating the supporting electrolyte as a binary electrolyte as a first approximation. Because the concentration of potassium hydroxide in the model pore was nearly an order of magnitude greater than that of the potassium zincate[18], the model follows this suggestion by treating the potassium hydroxide as a binary electrolyte, independent of the zincate ions present.

---

[18] The electrolyte used here was 31 wt% potassium hydroxide saturated with zinc oxide. The equilibriated solution had actual concentrations of approximately 5.6 M potassium hydroxide and approximately 0.7 M potassium zincate.

In accord with another assumption of Levich's first approximation, this model allows the zincate ion to move by diffusion only, without any contribution from migration. This is justified by the small percentage of current the zincate ions carry. For this system, the transference number of the zincate ion is below 0.05 before anodic oxidation commences (i.e. when the zincate ion concentration is no higher than its saturation value). Even at the maximum zincate ion concentration expected for the probe beam deflection experiments (as calculated by the model), the zincate ion transference number remains below 0.07. Furthermore, the numerical results of Mak and Cheh (28) - which incorporate the effect of migration in a semi-infinite geometry - suggest that the surface concentration of hydroxide ion should remain large in comparison with the concentration of zincate ion for sufficiently concentrated solutions (greater than 2N KOH). Thus, the time-dependent diffusion equation (Eq. [8]) should provide a good approximation for the movement of zincate ions.

Based upon the coordinates shown in Fig. 11, the boundary conditions at the electrodes are

$$\frac{\partial c_1}{\partial y} = \frac{s_1 i_n}{n F D_1} \qquad [9a]$$

$$\frac{\partial c_2}{\partial y} = \frac{s_2 t_{K^+} i_n}{n F D_2} \qquad [9b]$$

Where i_n is the transfer current density in the pore, s_i is the stoichiometric coefficient, n is the number of electrons transferred in the reaction, D_1 is the diffusion coefficient of zincate ion, D_2 is the effective diffusion coefficient

of potassium hydroxide, and t_{K^+} is the transference number for potassium ions[19]. The remaining boundaries are insulators

$$\frac{\partial c_1}{\partial y} = \frac{\partial c_2}{\partial y} = 0; \quad \text{at YR=1 for all XR, and at YR=0 for } 1.0<XR<1.14 \qquad [10a]$$

$$\frac{\partial c_1}{\partial x} = \frac{\partial c_2}{\partial x} = 0; \quad \text{at XR=0 for all YR, and at XR=2.14 for all YR} \qquad [10b]$$

3. Transfer Current Density Distribution

The transfer current density employed in the electrode boundary conditions varies as a function of position according to the one-dimensional secondary current distribution for a single electrode. The analytic description of this distribution was originally obtained by Euler and Nonnenmacher (29,30) for a single macroscopic porous electrode[20]. By

---

[19] The potassium ion transference number appears in Eq. [9b] because migration is included in the flux boundary condition. The boundary expression was obtained by setting the flux of potassium ions equal to zero at the electrode. From this, an expression for the potential gradient at the electrode was obtained which was then substituted into the hydroxide-ion flux expression.

[20] In the limit of infinite electrode conductivity, the one-dimensional mathematical formulation for the macroscopic porous electrode is equally applicable to a one-dimensional version of the model pore.

assuming a linear relationship between the charge transfer overpotential and the transfer current density, they arrived at the following expression:

$$\frac{i_n}{i_{avg}} = \nu \frac{\cosh(\nu \cdot XR)}{\sinh(\nu)} . \qquad [11]$$

Here i_{avg} is the transfer current density averaged over the model pore electrode surface area, and ν is a dimensionless parameter representing the relative importance of ohmic and charge transfer resistances

$$\nu = L \sqrt{\frac{i_0 \, n \, F}{R \, T \, \kappa \, d}} . \qquad [12]$$

In this expression, i_0 is the exchange current density, L is the electrode length (axial direction), d is the cell height (radial direction) and, κ is the electrolyte conductivity. Typically, the current density distribution on an electrode is described in terms of the Wagner number. This dimensionless number is defined as the ratio of the charge transfer resistance to the ohmic resistance in the electrolyte (45) and may be written as follows:

$$W = \frac{\partial \eta}{\partial i_n} \frac{\kappa}{L^*} \qquad [13]$$

Here η is the surface overpotential and L^* is the characteristic length of the cell[21]. It should be noted that the parameter ν appearing in the one-

---

[21] The height of the cell, d, and the electrode length, L, are of comparable magnitude and should therefore both appear in the characteristic length. By expressing the surface

dimensional current density expression is the square root of the reciprocal Wagner number.

Because a one-dimensional transfer current distribution does not completely account for the two-dimensional character of the model pore, a two-dimensional numerical model was developed for comparison. The two-dimensional secondary current distribution was obtained by solving Laplace's Equation in the model pore geometry, using the Butler-Volmer kinetic expression at the electrode boundaries. In dimensionless form, these expressions take on the following form:

$$\varepsilon^2 \frac{\partial^2 U}{\partial XR^2} + \frac{\partial^2 U}{\partial YR^2} = 0 \qquad [14]$$

$$\frac{\partial U}{\partial YR} = -Ja[\exp(\alpha_a(V-U)) - \exp(-\alpha_c(V-U))] \qquad [15]$$

The dimensionless parameters used in these expressions are given by the following expressions:

$$U = \frac{nF}{RT}\Phi \qquad [16]$$

---

and ohmic resistances separately and writing the Wagner number as their ratio, the characteristic length can be shown to be $L^* = \frac{L^2}{d}$.

$$V = \frac{n\,F}{R\,T} v \qquad [17]$$

$$Ja = \frac{i_0\,(\alpha_a + \alpha_c)\,n\,F\,d}{\kappa\,R\,T} \qquad [18]$$

$$\varepsilon = \frac{d}{L} \qquad [19]$$

In the above expressions[22], v is the uniform zinc electrode potential, Φ is the electrolyte potential, α_a and α_c are the transfer coefficients for the anodic and cathodic reactions. The Galerkin finite element method (FEM) (31,32,33) was used to arrive at a numerical solution to the problem. Rectangular elements were used with biquadratic basis functions, and numerical integration was accomplished using 3-point Gaussian quadrature. We used a Newton-Rhapson iterative approach to promote convergence of the potential problem. Since the model pore experiments were conducted galvanostatically, iteration to a constant-current solution was also necessary. This was accomplished by adjusting the electronic potential of the cathode after each solution to the potential problem. To accelerate convergence to the constant-current solution, we employed a first-order continuation scheme (34).

---

[22]In terms of these dimensionless quantities, the Wagner number is approximated by ε^2/Ja.

4. Solution Technique

The mass transfer equations together with the stated boundary conditions[23] were solved for the two-dimensional model pore geometry using an alternating direction implicit finite difference routine (35,36). In order to compare the experimental results with the calculated values, refractive index gradients were calculated at various positions within the model pore. The calculated refractive index gradient is obtained by simply summing the refractive index gradient contribution of each solute species, which is in turn derived from the respective concentration gradients:

$$\frac{\partial n}{\partial y} = \frac{\partial c_1}{\partial y} \cdot \frac{\partial n}{\partial c_1} + \frac{\partial c_2}{\partial y} \cdot \frac{\partial n}{\partial c_2} \qquad [20]$$

Because the refractive index gradient may vary slightly across the probe laser beam diameter, the numerical model calculates a gaussian-weighted average of the refractive index gradients over the $1/e^2$ probe beam area to more-accurately reflect the experimental conditions.

---

[23] The mass transfer boundary conditions at the electrodes were obtained from the time invariant secondary current distribution described above.

C. Comparison of Experimental and Theoretical Results

Table 2 presents the parameter values used in this model. The literature values for most of these parameters vary considerably. Those used in the mathematical model were chosen because they provided good agreement between the numerical and experimental results, while remaining within the range of reported results. However, the value we chose for the diffusivity of potassium hydroxide is somewhat smaller than widely-cited values; the experimental values follow an unexpected trend toward greater diffusivity with increasing concentration (37). The diffusion coefficient employed in the present model was instead obtained by correcting the infinitely dilute solution value (2.85×10^{-5} cm^2/s) (38) to correspond to a concentrated solution. The correction was made by assuming that diffusivities of ionic species are inversely proportional to solution viscosity and directly proportional to the absolute temperature (38) (i.e. $\frac{D\mu}{T}$ = constant).

Figure 12 presents a comparison between the one- and two-dimensional current density distributions for a cell having the model pore geometry and the physical properties of a zinc electrode in alkaline electrolyte. When the reaction is symmetric (i.e. $\alpha_a = \alpha_c$), the two current density distributions closely agree. For the asymmetric current density distribution ($\alpha_a \neq \alpha_c$), the one-dimensional solution will agree with the two-dimensional solution only if a different value of the parameter ν is chosen for each electrode. This is necessary because the one-dimensional solution

Table 2

Values for the parameters used in the calculations

Parameter	Value	Reference
Diffusivity of KOH	1.2×10^{-5} cm^2/s	[38]
Diffusivity of zincate ion	8×10^{-6} cm^2/s	[11, 39]
Exchange current density (i_0)	0.8 mA/cm^2	[40,41]
Electrolyte conductivity (κ)	0.46 $(\Omega\ \text{cm})^{-1}$	[42]
Anodic transfer coefficient (α_a)	0.75	[43,44]
Cathodic transfer coefficient (α_c)	0.25	[43,44]
Beam distance from electrode	0.011 cm	—
Beam radius	40μm	—

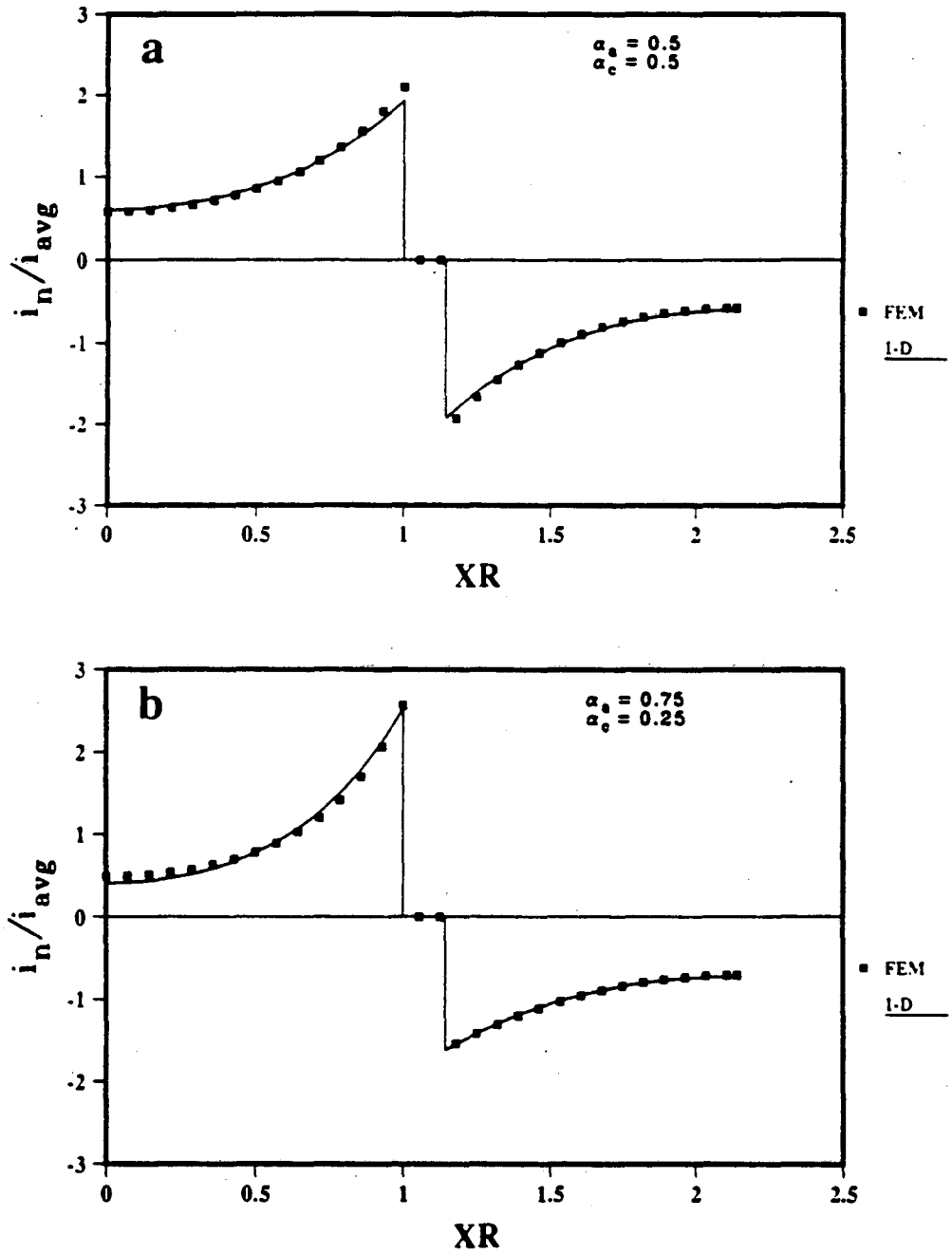

Figure 12. Comparison of the finite element method (FEM) two-dimensional solution (squares) and the one-dimensional analytic solution (solid curves) in dimensionless format for (a) a symmetric current distribution ($\alpha_a = \alpha_c$), and (b) an asymmetric current distribution ($\alpha_a \neq \alpha_c$). In both cases W = 0.3 for the FEM distribution. In the asymmetric case, however, two different values of v were required for the analytic solution (v_{anodic}=2.51 and $v_{cathodic}$=1.45)

is derived for a single electrode and assumes linear kinetics. Since the transfer coefficients do not appear independently in the expression for linear reaction kinetics, it is impossible to represent an asymmetric reaction distribution across two electrodes. Thus, the value of ν is adjusted to, in effect, account for the unequal values of the transfer coefficients.

Figure 13 shows that the agreement between the two descriptions of current distribution will break down under some conditions. This is important because various investigators have considered the one-dimensional distribution in their treatment of the reaction distribution in porous zinc electrodes (1,15,18). Yet, the individual pores of a porous electrode will not all possess the long, thin geometry assumed for the one-dimensional current density distribution. The agreement between the two distributions can be conveniently described in terms of the Wagner number. As Fig. 13 shows, the one-dimensional solution, Eq. [11], predicts a current distribution that is more uniform than the solution to the two-dimensional problem, Eq. [14], at high Wagner numbers. Thus, the use of a two-dimensional distribution becomes increasingly necessary as Wagner number increases, e.g. as the pore diameter grows with respect to the pore depth, or the exchange current density decreases.

By employing the asymmetrical current distribution shown in Fig 12b, the concentration profiles shown in Fig. 14 are obtained. Figure 14 shows that between the dimensionless positions XR=0.75 and XR=1.00, the

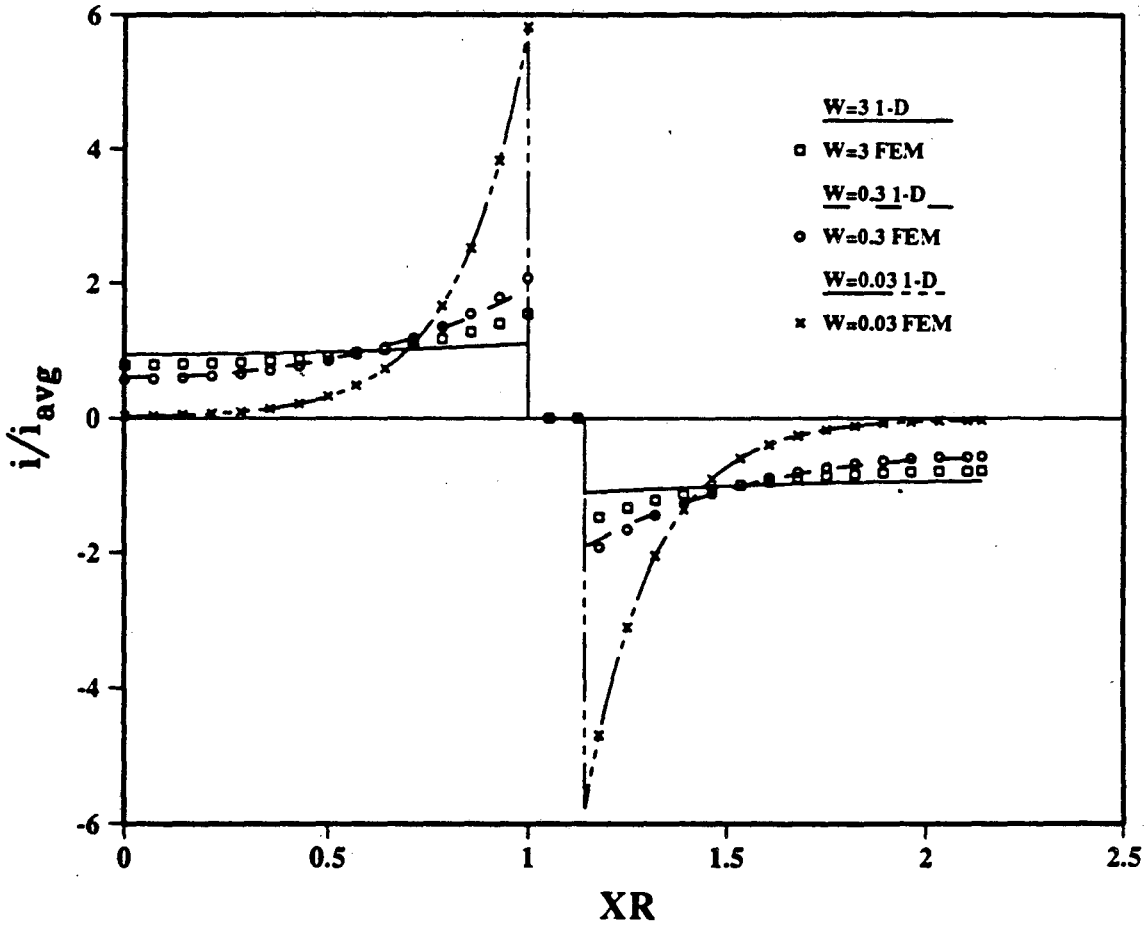

Figure 13. Comparison of the two-dimensional FEM and the one-dimensional analytic solutions for three Wagner numbers.

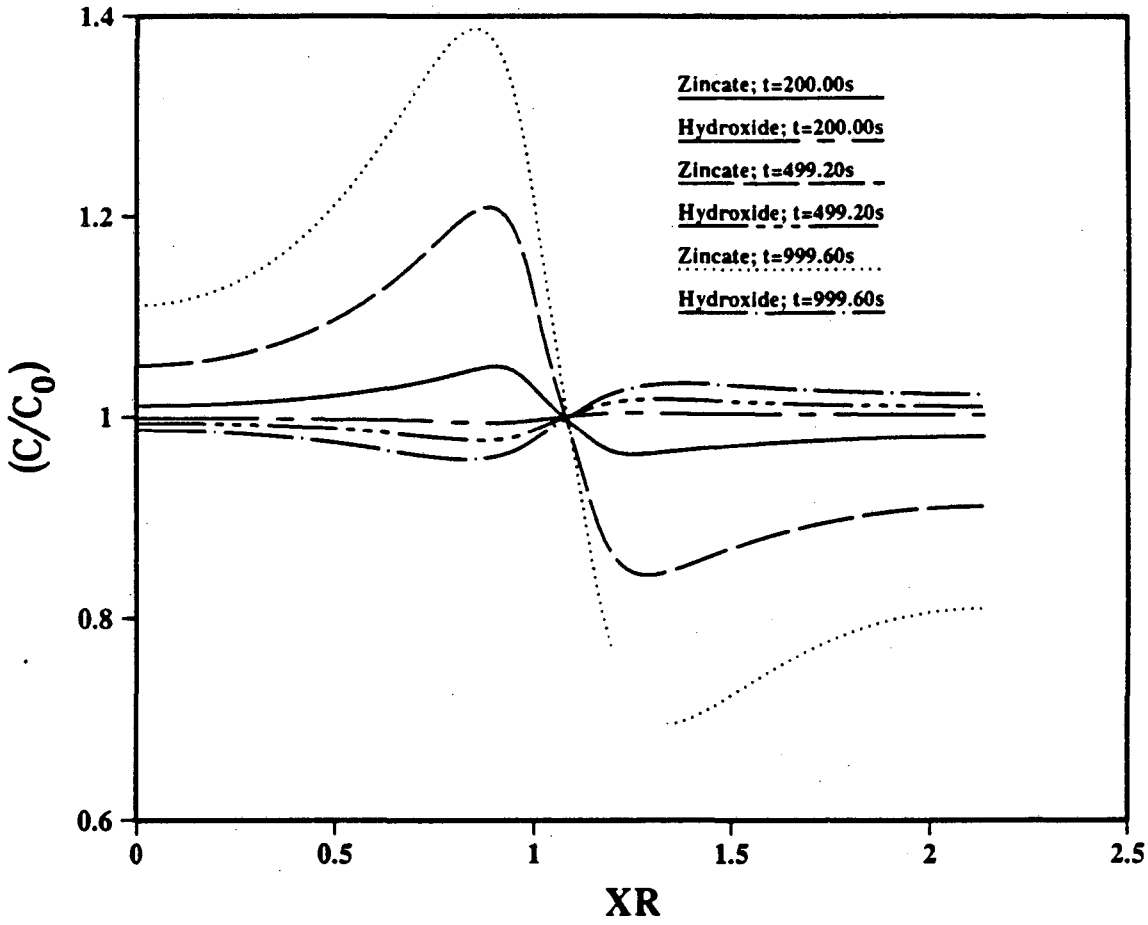

Figure 14. Calculated concentration distributions of KOH and $K_2Zn(OH)_4$ along the horizontal plane at YR=0.55 for α_a=0.75, α_c=0.25 and .50 mA total cell current.

calculated concentration of zincate grows to a maximum and that of hydroxide drops to a minimum. Thus, if the numerical model accurately describes the conditions within the model pore, the experimentally observed axial component of the refractive index gradients - and thus the zincate ion concentration gradient - will change direction near the pore mouth. The experimental results presented in Fig. 15 show that the sign of the refractive index gradient does indeed change from negative to positive between XR=1.00 and XR=0.75, as expected. Other aspects of the observed probe beam deflection results are also described accurately by the numerical model. For instance, the relative size and time dependence of the calculated axial-direction refractive index gradients compare well with the experimental results shown in Fig. 15[24].

Figure 16 shows that the experimental and numerical results for the normal component of the refractive index gradients have the same general time-dependent shape. Both experimental and numerical results show that these refractive index gradients grow rapidly for approximately 20 seconds and then approach a nearly steady value until the current is interrupted. The absolute values of the measured refractive index gradient

---

[24] As pointed out in Chapter II, the flat region on the curve at XR=1.00 resulted from a large-gradient deflection that moved the laser beam beyond the edge of the position detector.

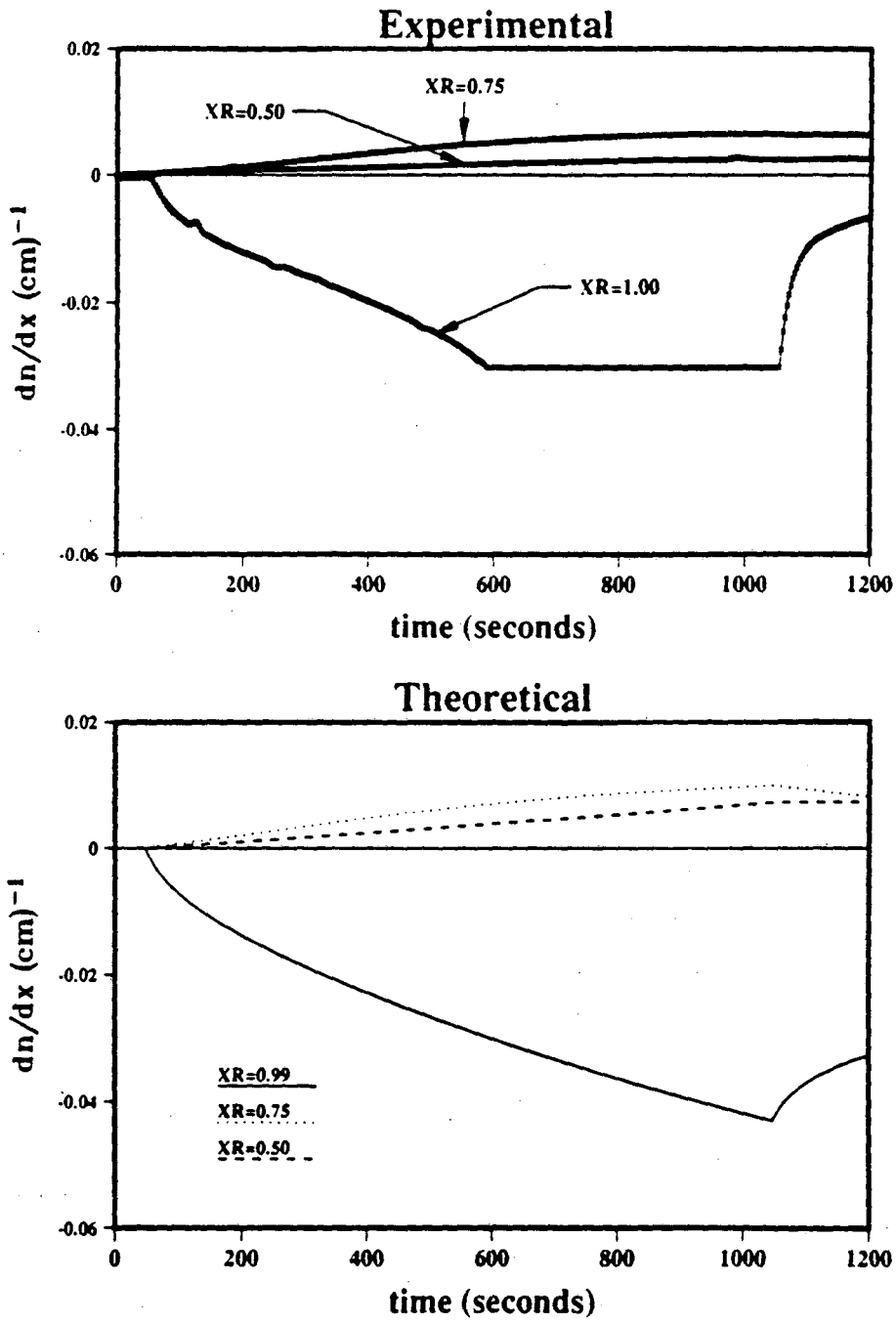

Figure 15. Comparison of the axial component of the refractive index gradient for typical experimental measurements and theoretical calculations. In both cases, 0.5 mA is passed for a total of 1000 s, from 45 to 1045 s.

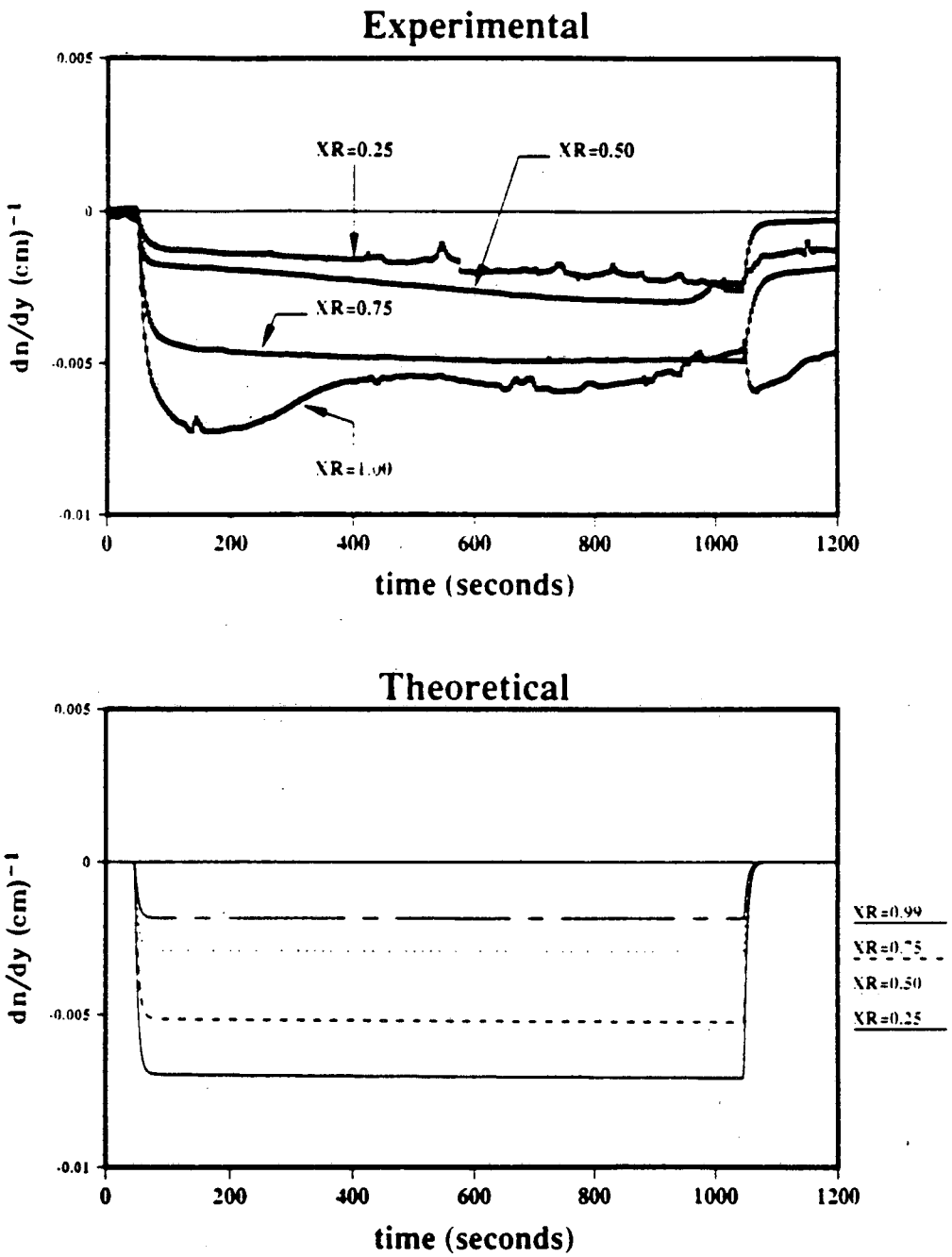

Figure 16. Comparison of the radial component of the refractive index gradient for typical experimental measurements and theoretical calculations. In both cases 0.5 mA is passed for a total of 1000 s., from 45 to 1045 s.

also agree well with the computed values as shown in Fig. 16. As Fig. 17 shows, the concentration distribution in the direction normal to the model pore electrode is expected to rapidly (within approximately 10 s after current begins passing) assume a parabolic profile[25] and then retain that shape throughout the course of the experiment. This parabolic shape explains why the measured deflection is strongly influenced by the distance from the electrode surface that the beam is placed. These curves also show that the concentrations of the electrolyte species continue to grow or decline so long as current is passing through the cell. However, because the shape of the concentration profiles does not change appreciably after the first few seconds, the gradients will remain relatively constant. This is in contrast to the gradients in the axial direction which continue to grow throughout the course of the experiment[26].

The current distribution employed in the numerical model strongly influences the calculated distribution of refractive index gradients within the model pore. The relative positions of the horizontal segments of the

---

[25] In the limit of diffusion between an infinitely long electrode and a parallel infinitely long insulator, the one-dimensional concentration distribution assumes a parabolic profile after a short time (46).

[26] This might be expected because the diffusional relaxation time (L^2/D) is greater in the axial direction than in the radial direction.

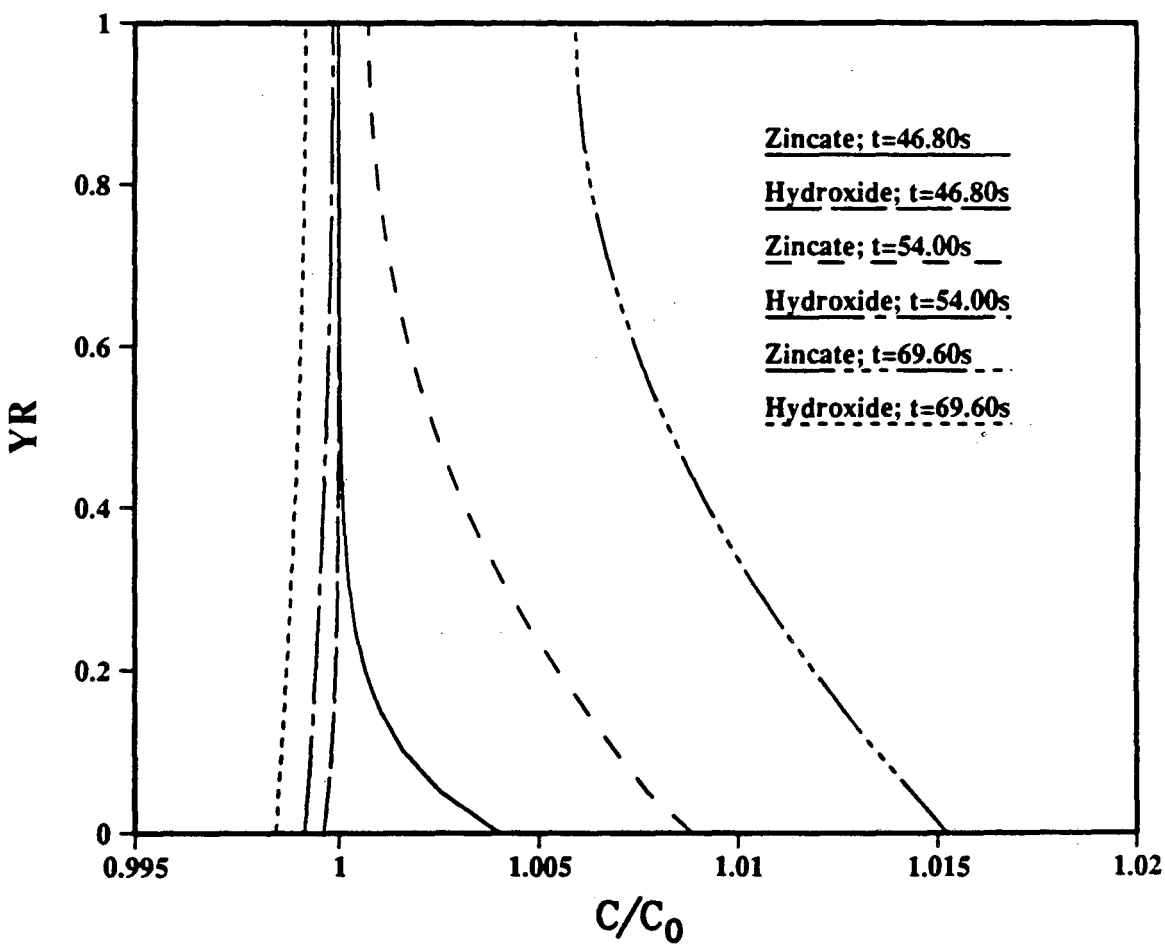

Figure 17. Calculated concentration profiles in the direction normal to the model pore electrode. The profiles were calculated for the conditions set forth in Table 2 at a beam position of XR = 0.75 and 0.5 mA total cell current.

gradient curves shown in Fig. 16 are a manifestation of the current density distribution. Because the reaction rate is greater near the model pore mouth, the concentration gradients are somewhat larger there. This is further illustrated in Fig. 18 by the observed radial-direction gradients at four beam positions and the corresponding calculated gradient distributions. The agreement between the model and the average values of the measured refractive index gradients is quite good for a total cell current of 0.5 mA. However, for higher total currents, the calculated gradients are significantly larger than the experimentally observed values. This discrepancy may be attributable to a partial beam reflection within the cell (as described in Chapter II) due to large beam deflections.

The current distributions that provide the best agreement with the experimental results suggest that much of the reaction within a pore takes place near the mouth of the pore, especially during discharge. This is in agreement with the experimental results of Liu *et al.* (18) and Yamazaki and Yao (24) for an array of cylindrical pores and with the results of Katan *et al.* (3) and Flatt *et al.* (1) for a single model pore. Experimental studies of actual porous zinc electrodes, however, sometimes suggest that the reaction distribution is more uniform (15). There are at least two possible reasons for expecting a more-uniform current density distribution than that predicted by the model or observed in the model pore. First, the precipitation present in a regular porous electrode may act to increase the local overpotential of the electrode, resulting in a more-uniform reaction distribution (15). Second, the net conversion of matrix material from zinc to zinc oxide should lower the matrix phase conductivity. Hence, more of the

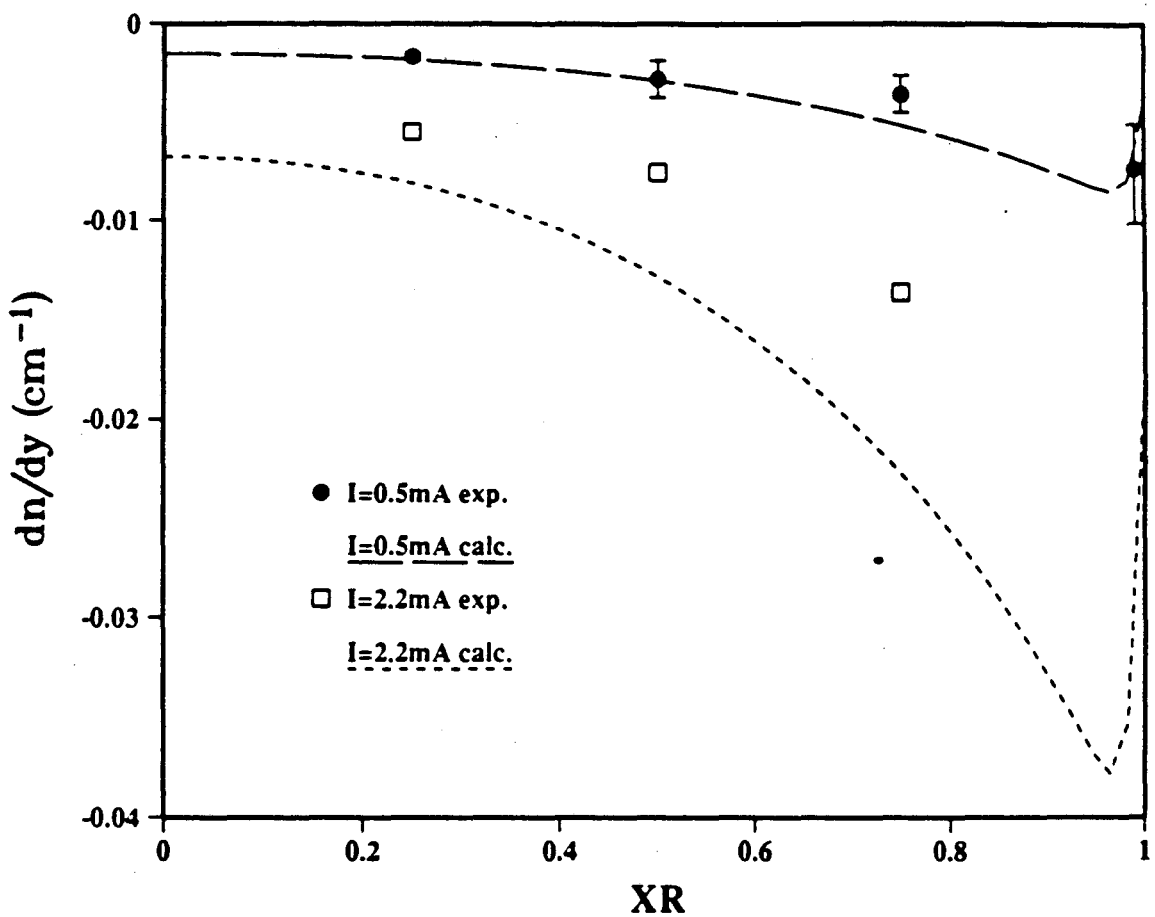

Figure 18. Variation of the normal component of refractive index gradient (measured at 100 s., and YR = 0.55) with distance. The results for a total current of 0.5 mA and 31wt% potassium hydroxide electrolyte represent averages of between 5 and 35 experiments conducted for each beam position. The error bars associated with each of these results represent the standard deviation from the average value.

current would be carried by the solution as the reaction progresses, thereby shifting the reaction profile toward the root of the pore.

The comparison between a macroscopic porous electrode and the model pore should be made with caution. As mentioned earlier, some of the mathematical descriptions of a model single pore and a macroscopic porous electrode are equivalent. Physically, however, there are many differences. In moving across the width of a porous electrode, several pores of various orientations may be encountered. Thus, it is possible that the reaction distribution we observed in the model pore accurately depicts the conditions within some single pores, but not within an entire electrode. If an actual porous electrode is treated as a distribution of numerous single pores in which precipitation can occur, a good macroscopic representation could be obtained. This might be accomplished, for example, by modelling the entire porous electrode as a solid matrix in which there is a random arrangement of single pores having varying sizes and orientations.

In so far as precipitation is concerned, the numerical model suggests that both type I and type II precipitation might be expected within a zinc electrode pore. As mentioned above, the calculated concentration of zincate reaches a maximum between XR=1.00 and XR=0.75. Therefore, diffusion is driving potassium zincate away from, and potassium hydroxide into this region. However, this transport is not sufficiently fast to prevent the accumulation of zincate and depletion of hydroxide near the pore mouth. As shown in Fig. 13 and Fig. 17, the concentrations of potassium zincate and potassium hydroxide in the anodic region continue to grow and decrease with time, respectively. This suggests that the potassium zincate

concentration near the pore mouth reaches supersaturation and could lead to type I precipitation within the electrolyte[27] (47,48). Also, the decrease of potassium hydroxide concentration might lead to passivation of the zinc electrode and the formation of a tightly adherent type II film (3).

D. Summary & Conclusions

The theoretical approach set forth here shows good quantitative agreement with the experimental results obtained by the probe beam deflection technique. Thus, probe beam deflection has proven to be a useful technique for investigating mass transfer within the electrolyte phase of a model single pore. The agreement between model and experiment also indicates that an adequate accounting for the behavior of a single pore has been included in the model. Extension of this single-pore model to the description of a full porous electrode is a logical next step in future work.

These results indicate that during the discharge of a zinc electrode the concentration of zincate within the model pore grows faster than it can be reduced by transport out of the pore. Likewise, the concentration of hydroxide ion continuously decreases within the model pore. These results suggest that under high-current conditions, type I and type II precipitates

---

[27] Some investigators have reported that type I, flocculating precipitate will begin to form when the zincate ion concentration reaches three times the saturation value. (47,49)

should form within the pores of a zinc electrode, as has been observed in porous zinc electrodes.

Finally, the agreement between the current distributions predicted by the frequently-used one-dimensional analytic model (originally developed by Euler and Nonnenmacher), and the more-rigorous two-dimensional finite element method, show that the one-dimensional model is in some instances a valid means of describing the potential distribution within a given range of variables. However, when the Wagner number is much larger than 0.3, the accuracy of the one-dimensional approach is reduced.

References

1. J.Flatt, F.R.McLarnon, and E.J.Cairns "Optical and Electrochemical Study of Model Zinc Electrode Pores in Alkaline Electrolyte" Lawrence Berkeley Laboratory Report No. LBL -20025 (1985)

2. J.O'M.Bockris and A.K.N.Reddy, "Modern Electrochemistry", Plenum Press, New York (1970)

3. T.Katan, J.R.Savory, and J.Perkins, *J. Electrochem. Soc.* **126**, 1835 (1979)

4. R.H.Muller, in *Advances in Electrochemistry and Electrochemical Engineering*, Delahay and Tobias, eds., **9**, *Wiley-Interscience, New York* , 1973, p.285

5. F.R.McLarnon, R.H.Muller, and C.W.Tobias, *J. Electrochem. Soc.* **122**, 59 (1975)

6. C.C.Jan, and R.L.McCreery, *Anal. Chem.* **58**, 2771 (1986)

7. R.E.Russo, F.R.McLarnon, J.D.Spear,and E.J.Cairns, *J. Electrochem. Soc.* **134**, 2783 (1987)

8. B.S.H.Royce, D.Voss, and A.Bocarsly, *J. DePhysique* **C6**, 325 (1983)

9. M.A.Tamor, and M.Zanini, *J. Electrochem. Soc.* **133**, 1399 (1986)

10. J.Pawlisyn, M.F.Weber, M.J.Dignam, A.Mandelis, R.D.Venter, and S.Park, *Anal. Chem.* **58**, 236 (1986)

11. J.McBreen and E.J.Cairns, "The Zinc Electrode", in *Advances in Electrochemistry and Electrochemical Engineering*, H.Gerischer and C.W.Tobias, Eds., Vol. 11, Wiley, New York, 1978.

12. J.T.Nichols, F.R.McLarnon, and E.J.Cairns, "Active Material Redistribution Rates in Zinc Electrodes: Effect of Alkaline Electrolyte Compositions having Reduced Zinc Oxide Solubilities", Lawrence Berkeley Laboratory Report No. LBL-17397 (1983)

13. T.C.Adler, F.R.McLarnon, and E.J.Cairns, "Improvements to the Cycle-life Performance of the Zn/NiOOH Cell", Proc. 22nd Intersociety Energy Conversion Engineering Conference, pp. 1097-1101, American Institute of Aeronautics and Astronautics, New York (1987)

14. R.W.Powers, and M.W.Breiter, *J. Electrochem. Soc.* **116**, 719 (1969)

15. Z.Nagy and J.O'M.Bockris, *J. Electrochem. Soc.*, **119**, 1129 (1972)

16. R. de Levie, "Electrochemical Response of Porous and Rough Electrodes," in *Advances in Electrochemistry and Electrochemical Engineering*, C.W.Tobias and H.Gerischer, eds. **6**, 329 (1967)

17. J.S.Dunning, D.N.Bennion, and J.Newman, *J.Electrochem.Soc.* **120**, 906 (1973);

18. M.B.Liu, G.M.Cook, and N.P.Yao, *J.Electrochem.Soc.* **129**, 239 (1982)

19. J. Newman and W. Tiedemann, *Am.Inst.Ch.Eng.J.* **21**, 25 (1975)

20. W.G.Sunu, and D.N.Bennion *J.Electrochem.Soc.* **127**, 2007 (1980)

21. F.M.Delnick, and R.A.Guidotti *J.Electrochem.Soc.* **137**, 11 (1990)

22. M.J.Isaacson, F.R.McLarnon, and E.J.Cairns *J.Electrochem.Soc.* **137**, 2014 (1990)

23. T.Katan, and H.F.Bauman, *J.Electrochem.Soc.* **122**, 77 (1975)

24. Y.Yamazaki and N.P.Yao, *J.Electrochem.Soc.* **128**, 1655 (1981)

25. E.C.Hume, W.M.Deen, and R.A.Brown *J.Electrochem.Soc.* **131**,1251 (1984)

26. R.Morris and W.Smyrl, *J.Electrochem.Soc.* **136**, 3229 (1989)

27. V. Levich, "The Theory of Concentration Polarization," *Acta Physicochimica U.R.S.S.*, **17**, 257-307 (1942)

28. C.Y.Mak and H.Y.Cheh, *J.Electrochem.Soc.* **135**, 2262 (1988)

29. J.Euler and W.Nonnenmacher, *Electrochim. Acta* **2**, 268 (1960)

30. J.S.Newman and C.W.Tobias, *J.Electrochem.Soc.* **109**,1183 (1962)

31. J.N.Reddy, "An Introduction to the Finite Element Method," McGraw-Hill, Inc. (1984)

32. R.Alkire, T.Bergh, and R.L.Sani, *J.Electrochem.Soc.* **125**, 1981 (1978)

33. R.Morris and W.Smyrl *Am.Inst.Ch.Eng.J.* **34**, 723 (1988))

34. Personal Communication, D.Graves (1990)

35. L.Lapidus and G.F.Pinder "Numerical Solution of Partial Differential Equations in Science and Engineering" John Wiley and Sons, Inc., New York (1982)

36. D.W.Peaceman and H.H.Rachford *J.Soc.Indust.Appl.Math.* **3**, 28 (1955)

37. R.N.Bhatia, K.E.Gubbins, and R.D.Walker, *Trans. Faraday Soc.* **64**, 2091 (1968)

38. J.Newman, "Electrochemical Systems," Prentice-Hall Inc., Englewood Cliffs, NJ (1973)

39. T.P.Dirkse, in *Power Sources 3*, 485, P.H.Collins, Ed. Oriel Press, Newcastle (1971)

40. L.A.Reznikova, D.P.Aleksondrova, and B.N.Kabanov, *Elektrokhimiya* **16**, 576 (1980)

41. K.G.Miller, E.J.Cairns, and F.R.McLarnon, Unpublished Data (1990)

42. T.P. Dirkse, "Electrode Migration and Reaction Processes Occurring within Alkaline-Zinc Batteries" NTIS Technical Report No. AFAPL-TR-69-90 (1969)

43. J.Hendrikx, A.VanDerPutten, W.Visscher, and E.Barendrecht, *Electrochim. Acta* **29**, 81 (1984)

44. J.O'M.Bockris, Z.Nagy, and A.Danjanovic, *J.Electrochem.Soc.* **119**, 285 (1972)

45. N.Ibl, in*Comprehensive Treatise of Electrochemistry*, E.Yeager, J.O'M.Bockris, B.E.Conway, and S.Sarangapani, Eds., Plenum Press, New York (1983), v.6, p. 257.

46. J.Crank, "The Mathematics of Diffusion", 2d Ed. Clarendon Press, Oxford (1975)

47. T.P.Dirkse, *J.Electrochem.Soc.* **128** 1412 (1981)

48. J.McBreen, "Nickel/Zinc" *Power Sources for Electrical Vehicles*, ed. B.D.McNicol and D.A.J.Rand, pp. 541-72, Elsevier, Amsterdam, The Netherlands (1984)

49. A.G.Briggs, N.A.Hampson, and A.Marshall, *J.Chem.Soc.Faraday Trans.2*, **70**, 1978 (1974).

50. Handbook of Chemistry and Physics, 66th Ed., CRC Press, (1986)

Appendix I: Refractive Index Measurements

The refractive index of each of the components in alkaline zincate electrolyte was measured as a function of concentration[28]. All solutions were prepared from a concentrated potassium hydroxide solution (J.T. Baker, Inc. "Analyzed Reagent" potassium hydroxide, titrated as 11.72 M). Solutions of 3.03, 6.29, 7.14, 8.02, and 11.72 molar potassium hydroxide were prepared. The refractive index was measured at 25° C with a Bausch & Lomb Abbe refractometer using the 546 nm. line from a mercury lamp. For each measurement, an excess of the potassium hydroxide and potassium zincate solutions was necessary, and scrupulous cleaning was required afterward. The potassium zincate solutions were prepared by dissolving varying amounts of zinc oxide in the potassium hydroxide solutions, being sure to maintain a final potassium hydroxide concentration of 5.5 M. To make these solutions, all dissolved zinc was assumed to be in the tetrahedrally bound potassium zincate form, $K_2Zn(OH)_4$.

---

[28] The refractive index of potassium hydroxide at 20° C using the sodium yellow light for various concentrations has been reported in reference 50. The results tabulated there agree with those obtained in our laboratory when the different experimental conditions are taken into account.

For zincate solutions, the value of 5.5 M free potassium hydroxide was chosen because it is a realistic representation of the electrolyte concentrations used in this study. A 7.14 M potassium hydroxide solution (31 wt %) saturated with zinc oxide yields a free hydroxide concentration of approximately 5.75M. Since hydroxide ions are consumed at the zinc anode, a slightly lower local concentration is expected there. The 5.5 M concentration also ensures that a sufficient amount of zinc oxide dissolves[29] and that the dissolved zinc species exist almost entirely in the tetrahedrally bound zincate configuration (11).

Plots of the data taken from these measurements together with the associated curve fits are shown in Figs. A1 & A2. As these plots show, the concentration dependence of refractive index is nearly linear. However, cubic and square fits give very good agreement and yield the following expressions (1 represents potassium hydroxide and 2 represents potassium zincate):

$$n_1 = 1.334+0.01076(c_1) - 4.267 \times 10^{-4}(c_1)^2 + 1.106 \times 10^{-5}(c_1)^3 \qquad [A1]$$

$$n_2 = 1.382+0.0190(c_2) + 2.961 \times 10^{-3}(c_2)^2 \qquad [A2]$$

---

[29] Zinc oxide is only sparingly soluble in neutral solutions (2×10^{-5}M), but its solubility follows an approximately square dependence on KOH concentration.

$$\frac{\partial n}{\partial c_1} = 0.01076 - 8.534 \times 10^{-4}(c_1) + 3.318 \times 10^{-5}(c_1)^2 \qquad [A3]$$

$$\frac{\partial n}{\partial c_2} = 0.0190 + 5.922 \times 10^{-3}(c_2) \qquad [A4]$$

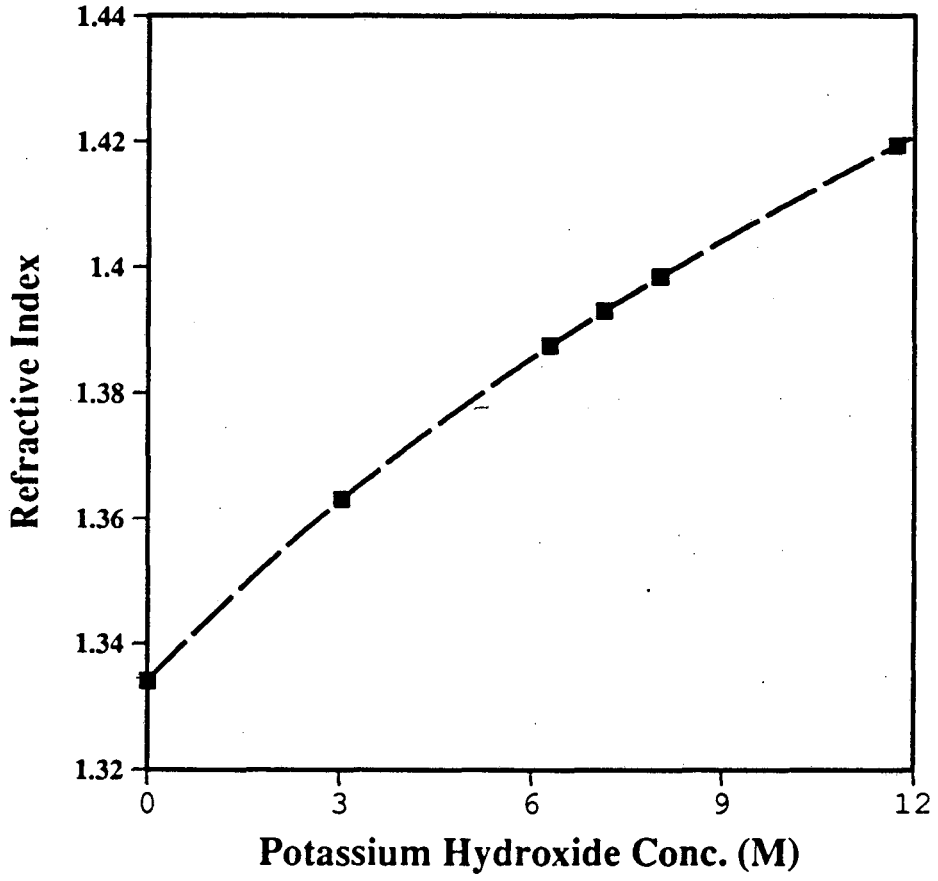

Figure A1. The dependence of refractive index on KOH concentration at 25°c. The curve is a cubic fit of the six data points shown.

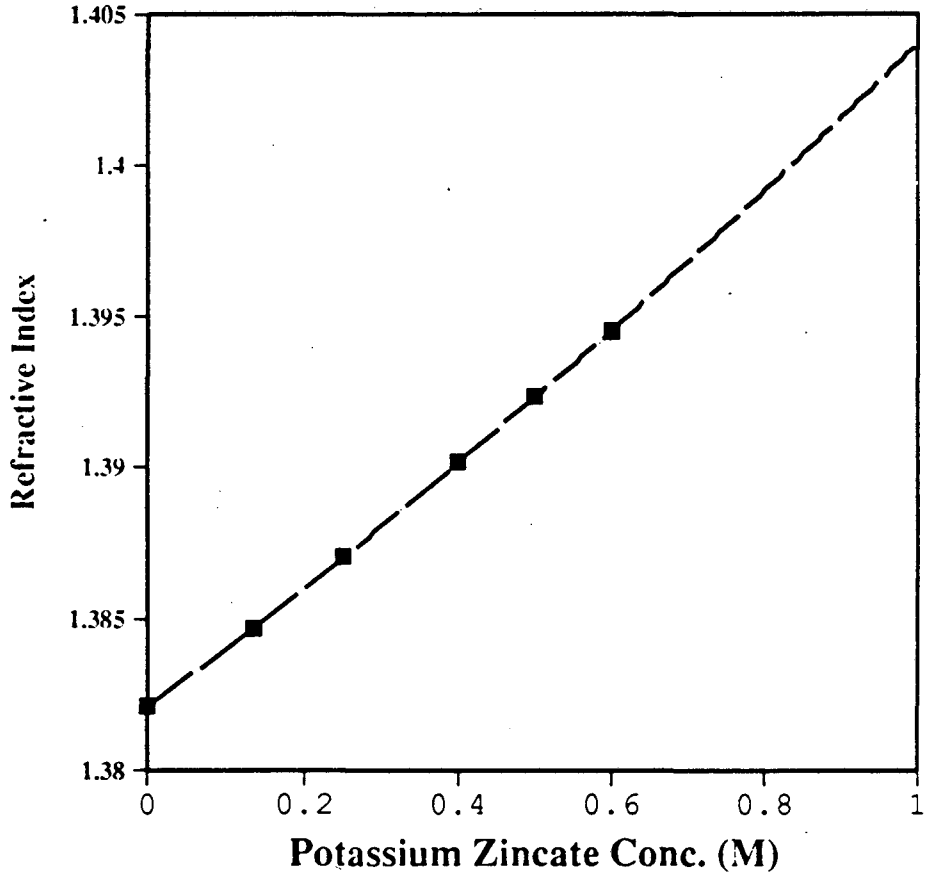

Figure A2. The dependence of refractive index on $K_2Zn(OH)_4$ concentration in electrolytes having a true concentration of 5.5 M free KOH, at 25°c. The curve is a square fit of the six data points shown.

Appendix II: Current Distribution Model

Set forth in this appendix is the code used to model the potential and current distributions within the model pore. Laplace's equation is solved with the Butler-Volmer surface overpotential expression as the electrode boundary condition. The output included the dimensionless potential in two dimensions throughout the cell and the dimensionless current over the electrodes. The code was written in Fortran 77 and compiled and ran on a DEC 6420 computer.

```
c   * This program solves the equation Uxx+Uyy+f(U)=0.
c   * It uses a Galerkin FEM routine with biquadratic basis functions.
c   * Numerical Integration is accomplished with a 3-point Gaussian
c     quadrature algorithm.
c   * A Newton-Rhapson iteration scheme is used to promote convergence
c     in non-linear problems.
c   * Another iteration is used to converge to a constant current
c     solution. Vcathode is varied after each iteration.
c   * First order continuation is used to promote rapid convergence
c     of the soln. to Poisson's Eq. for each new value of Vcathode.
c
      DIMENSION SJ(1089,1089),SR(1089),SA(1089),PHI(9),PHIC(9),PHIE(9)
      DIMENSION PHIX(1089),PHIY(1089),ph1d(3),U(1089),cur(1089)
      REAL*8 curr(121),dXR(60),dYR(4)
      DIMENSION DELTA(1089),nop(240,9),iw1(9)
      DIMENSION axpt(1089),aypt(1089),xpt(1089),YR(1089),XR(1089)
```

```
      DIMENSION GP(3),W(3)
      COMMON /WORKSP/ RWKSP
      REAL RWKSP(1188121)
      CALL IWKIN(1188121)
       open (unit=5,file='tu.out',status='unknown')
       open (unit=12,file='cur.out',status='unknown')
       open (unit=13,file='test.out',status='unknown')
       OPEN (UNIT=14,FILE='u.out',STATUS='UNKNOWN')
       OPEN (UNIT=16,FILE='cntr.out',STATUS='UNKNOWN')
c
c     enter modified gaussian quadrature coordinates and weighting
c     values. The tabulated weighting values are divided by 2
c     to account for the transformation from dE to dz.  The gauss points,z,
c     are modified to be expressed as E=(z+1)/2.
c
      DATA W/0.277777777778,0.4444444444,0.27777777778/
      DATA GP/0.112701666,0.5,0.887298335/
c
c     Is equation (and b.c.s) linear?  If yes, "lin"=1.  This will
c     avoid iterations so long as the residual disappears everywhere
c     but boundaries.
c
      lin=0
c
c     initial electrode kinetics and other parameters
c
      eL=0.7
```

```
      d=0.02
      en=2.
      F=96485.
      aRe=8.31439
      zkappa=0.46
      excur=0.0000795891
      temp=295.15
      TI=0.0005
       curavg=TI/eL
        aJ=excur*en*F*d/(aRe*temp*zkappa)
       epsiln=d/eL
      Va=0.00
      Vc=-2.8032
      alfa=0.75
      alfc=0.25
c
c     input number of elements and nodes
c
      nex=60
      ney=4
       ne=nex*ney
       nnx=2*nex+1
       nny=2*ney+1
        nn=nnx*nny
c
c     input step size and bottom y values and left x values for rectangle
c
```

```
      do 1 m=1,nex
 1    dXR(m)=2.1428571/60.
      do 2 m=1,ney
 2    dYR(m)=0.25
      ybcrd=0.0
      xlcrd=0.0
c
c     label global nodes (global node number (NOP) is identified in terms of
c     element number and local node number)
c
      do 3 i=1,nex
      do 3 j=1,ney
      nel=nel+1
      do 3 k=1,3
      l=3*k-2
        nop(nel,l)=nny*(2*i+k-3)+2*j-1
       nop(nel,l+1)=nop(nel,l)+1
 3     nop(nel,l+2)=nop(nel,l)+2
c
c     input x and y coordinates
c
         call rectg(nn,nny,dXR,dYR,eL,xlcrd,ybcrd,xpt,XR,YR)
c
c     Iterate to a constant current result.  Attempt to find
c     electrode potentials at which the total current
c     calculated by integrating the current density over the
c     face of the anode agrees with the galvanostatic current, TI.
```

```
c
      Vcg=-0.0
      Vcl=-0.0
910   ITC=ITC+1
      write (13,5)ITC*1.
      do 912 j=1,nn
912   DELTA(j)=0.0
c
c   count iterations for constant potential problem
c    and initialize matrices
c
      ITR=0
 50   ITR=ITR+1
      do 4 j=1,nn
      SR(j)=0.0
      SA(j)=0.0
      do 4 k=1,nn
 4    SJ(j,k)=0.0
c
c   FILL JACOBIAN AND RESIDUAL VECTOR
c
      DO 100 i=1,ne
c
c   convert global node numbers to local counterparts
c
      do 6 j=1,9
 6    iw1(j)=nop(i,j)
```

```
c
c   write x and y values of local nodes
c
    do 7 n=1,9
    j=nop(i,n)
    axpt(n)=XR(j)
 7   aypt(n)=YR(j)
c
c   loop over gauss points in two dimensions
c
    DO 100 j=1,3
    DO 100 k=1,3
      CALL TFUNCT(GP(j),GP(k),phi,phic,phie,ph1d)
c
c   set up isoparametric mapping routine
c
    xc=0.
    xe=0.
    yc=0.
    ye=0.
c   interpolate to dx/dE,dy/dC, etc. at each combination
c         of E and C Gauss Points
    do 120 n=1,9
     xc=xc+axpt(n)*phic(n)
     xe=xe+axpt(n)*phie(n)
     yc=yc+aypt(n)*phic(n)
120   ye=ye+aypt(n)*phie(n)
```

```
c    calculate jacobian for coordinate transformations
     det=xc*ye-xe*yc
c   compute the derivatives of phi with respect to x and y
    do 130 in=1,9
       phix(in)=(ye*phic(in)-yc*phie(in))/det
130     phiy(in)=(-xe*phic(in)+xc*phie(in))/det
c
c   compute guesses for U, Ux, and Uy by interpolating with
c        quadratic basis functions
c
    U1=0.
    U2=0.
    U3=0.
    do 90 n=1,9
     U1=U1+U(iw1(n))*phi(n)
     U2=U2+U(iw1(n))*phix(n)
 90   U3=U3+U(iw1(n))*phiy(n)
c
c   loop over local nodes to fill in the global residual vector
c
    do 100 l=1,9
       SR(iw1(l))=SR(iw1(l))-w(j)*w(k)*det*(epsiln**2*phix(l)
   1 *U2+phiy(l)*U3)
c
c    loop over local nodes again to fill in the global jacobian matrix
c
    do 100 m=1,9
```

```
      SJ(iw1(l),iw1(m))=SJ(iw1(l),iw1(m))+w(j)*w(k)*det*(phix(m)*
     1 phix(l)*epsiln**2+phiy(m)*phiy(l))
100   continue
c
c   BOUNDARY CONDITIONS
c
c   No essential boundary conditions in this problem.
c
c   At the top,right and left sides we have natural boundary
c   conditions with Ux=Uy=0. Thus there is no need to change the
c   Jacobian matrix or residual vector in these regions.
c   However, on the bottom we have a mixed b.c., Ux(x,0)=f(x,U).
c
c   Mixed boundary conditions on bottom of rectangle
c
c   loop over bottom side elements
c
      V=Va
      do 101 i=1,(ne-(ney-1)),ney
      if (i.eq.113) go to 101
      if (i.eq.117) go to 101
      if (i.eq.121) go to 101
      if (i.eq.125) go to 101
      if (i.gt.125) go to 103
      go to 102
103   V=Vc
102   continue
```

```
c
c   loop over 3 one-dimensional gauss points.  The basis functions will
c   be one-dimensional in the x direction at local nodes 1, 4, and 7.
c
c   calculate the one-D potentials at the boundary
c
    do 101 j=1,3
     call TFUNCT(GP(j),0.,phi,phic,phie,ph1d)
    U1=0.
    U2=0.
    U3=0.
    do 93 n=1,7,3
     U1=U1+U(nop(i,n))*phi(n)
     U2=U2+U(nop(i,n))*phix(n)
93   U3=U3+U(nop(i,n))*phiy(n)
c
c   loop over bottom three local nodes to augment the global residual vector
c
    do 101 l=1,7,3
       SR(nop(i,l))=SR(nop(i,l))+w(j)*dXR((i-1)/ney+1)*aJ*phi(l)
     1 *(exp(alfa*(V-U1))-exp((-alfc)*(V-U1)))
c
c   first order continuation vector
c
    if (V.ne.Vc) go to 140
       SA(nop(i,l))=SA(nop(i,l))+w(j)*dXR((i-1)/ney+1)*aJ*phi(l)
     1 *(alfa*exp(alfa*(V-U1))+alfc*exp((-alfc)*(V-U1)))
```

```
140   continue
c
      do 101 m=1,7,3
        SJ(nop(i,l),nop(i,m))=SJ(nop(i,l),nop(i,m))
        1 -w(j)*dXR((i-1)/ney+1)*aJ*(-phi(l))*phi(m)*(alfa*exp(alfa*(V-U1))
      2 +alfc*exp((-alfc)*(V-U1)))
101   continue
c
c   Solve matrix equation to get delta U
c
      IPATH=1
        CALL LSARG(nn,SJ,nn,SR,IPATH,DELTA)
c
c   convergence test and calculation of U for next iteration
c
      ERR=0.0
      DO 300 I=1,nn
      U(I)=U(I)+DELTA(I)
300     ERR=ERR+DELTA(I)**2
        ERR=SQRT(ERR/FLOAT(nn-1))
c
c   test progress of the convergence march
c
      if (lin.eq.1) go to 301
      IF (ERR .LT. 1.E-6) GO TO 301
      IF (ITR .GT. 5) GO TO 302
      write(13,5)ERR
```

```
c
c   loop back for next iteration on the potential problem
c
    go to 50
301   continue
c
c   calculate current at the bottom surface
c
    V=Va
     do 400 i=1,(nn-(nny-1)),nny
      if ((i.eq.nop(113,4)).or.(i.eq.nop(117,1)).or.
     1 (i.eq.nop(117,4)).or.(i.eq.nop(121,1)).or.(i.eq.nop(121,4))
    2 .or.(i.eq.nop(125,1)).or.(i.eq.nop(125,4))) go to 401
     if (i.gt.nop(125,4)) go to 403
    go to 402
403   V=Vc
402   continue
        cur(i)=excur/curavg*(exp(alfa*(V-U(i)))-exp((-alfc)*(V-U(i))))
    go to 400
401   cur(i)=0.0
400   continue
c
c   Integrate the current over anode using 3 pt. Gaussian quadrature.
c
    Tcur=0.0
    do 412 i=1,109,ney
    cur1=0.0
```

```
      DO 413 j=1,3
       CALL TFUNCT(GP(j),0.0,phi,phic,phie,ph1d)
      cur2=0.0
      do 91 l=1,7,3
 91     cur2=cur2+cur(nop(i,l))*phi(l)
413      cur1=cur1+w(j)*dXR((i-1)/ney+1)*cur2
412    Tcur=Tcur+cur1
       write (13,5) ITC*1.,Vc,Tcur
c
c   convergence algorithm to home in on the constant total
c   current.  This accomplished by adjusting the electronic
c   potential of the anode, Va, to increase or decrease the
c   total current passing through the cell.
c
      Vc0=Vc
       delI=1.0-Tcur
       if (sqrt(delI**2.).lt.1.e-3) go to 911
      if (delI.gt.0.0) go to 415
      Vcg=Vc
       Vc=(Vcg+Vcl)/2.
     go to 418
415    Vcl=Vc
       if (Vcg.eq.0.0) go to 416
       Vc=(Vcl+Vcg)/2.
     go to 418
416    Vc=1.2*Vc
418    continue
```

```
c
c   First order continuation calculation of new U(j)
c   Redefine SR vector as SA=(dRi/dVc)*deltaVc
c
    DVc=Vc-Vc0
    do 419 j=1,nn
419   SA(j)=SA(j)*DVc
      call LSARG(nn,SJ,nn,SA,IPATH,DELTA)
    do 420 j=1,nn
420   U(j)=U(j)+DELTA(j)
    go to 910
911 continue
c
c   Test for zero charge accumulation.  Total current leaving the
c   anode should equal the total current entering the cathode.
c
    Zcur=0.0
    do 414 i=129,237,ney
    cur1=0.0
    DO 417 j=1,3
     CALL TFUNCT(GP(j),0.0,phi,phic,phie,ph1d)
    cur2=0.0
    do 92 l=1,7,3
 92   cur2=cur2+cur(nop(i,l))*phi(l)
417   cur1=cur1+w(j)*dXR((i-1)/ney+1)*cur2
414 Zcur=Zcur+cur1
      ZT=sqrt(Zcur**2)-sqrt(Tcur**2)
```

```
      write (13,5) ZT,Zcur
      if (ZT.gt.1.e-2) go to 304
c
c  Write Output
c
 5  Format (3e14.5)
11   Format(1x,'title text is "Potential Distribution"
     1  '",f6.2,' iterations".')
40   Format(1x,'title text is "Current Distribution"
     1 "Cell Potential ',f6.2,' mV"
     2 "epsilon',f7.3,' Ja',f7.4,'".')
12    Format(1x,'xl is "XR distance".')
13    Format(1x,'yl is "U (volts)".')
14   Format(1x,'page-border is 0.')
15   Format(1x,'legend text is " ".')
16   Format(1x,'legend units are plot%.')
17   Format(1x,'legend box is 0.')
18   Format(1x,'legend x origin is 95.')
19   Format(1x,'legend y origin is 20.')
21   Format(1x,'input data.')
25    Format(1x,'"y=0"')
32    Format(1x,'"y=.5*top"')
33    Format(1x,'"y=top"')
      Write (14,11) ITR*1.
       Write (12,40) -Vc*1000.*aRe*temp/(en*F),epsiln,aJ
      Write (14,12)
      Write (12,12)
```

```
41    Format(1x,'yl is "i/iavg".')
      Write (12,41)
      Write (14,13)
      Write (14,14)
      Write (12,14)
      Write (14,15)
      Write (12,15)
      Write (14,16)
      Write (12,16)
      Write (14,17)
      Write (12,17)
      Write (14,18)
      Write (12,18)
      Write (14,19)
      Write (12,19)
      Write (14,21)
      Write (12,21)
      Write (14,25)
      do 22 j=1,nnx
22    write (12,5) XR((j-1)*nny+1),cur((j-1)*nny+1)
      do 37 j=1,(nn-8),nny
37    write (14,5) XR(j),U(j)
      write (14,32)
      do 30 j=5,(nn-4),nny
30    write(14,5) XR(j),U(j)
      write(14,33)
      do 31 j=nny,nn,nny
```

```
31    write(14,5) XR(j),U(j)
      do 38 k=1,nny
      ii=k
       iii=nn-(nny-k)
      do 38 j=ii,iii,nny
38     write(16,5)XR(j),YR(j),U(j)
23    Format(1x,'end data.')
27     Format(1x,'**file**')
      Write (14,23)
      Write (12,23)
      Write (14,27)
      Write (12,27)
      go to 29
c
c     Achtung! No convergence after 5 iterations
c
302   Write (14,28)
      go to 29
304   Write (12,36)
28     Format(1x,'Achtung! Has not converged')
34     Format(1x,'Achtung! No convergence to const. cur.')
36    Format(1x,'Achtung! Greater than 1% current mismatch
     1 between electrodes')
29    continue
      STOP
      END
c
```

```
c
*********************************************************************
c   subroutine to calculate 2-D quadratic basis functions
c
*********************************************************************
c
      SUBROUTINE TFUNCT(C,E,PHI,PHIC,PHIE,PH1D)
      DIMENSION PHI(9),PHIC(9),PHIE(9),PH1D(3)
c
c   define 1-D basis functions in terms of arbitrary variable, z.
c   z represents E or C, each of which range from 0 to 1 over element
c
      F1(Z)=2.*Z**2-3.*Z+1
      F2(Z)=4.*Z-4.*Z**2
      F3(Z)=2.*Z**2-Z
c
c   derivatives of 1-D basis functions
c
      DF1(Z)=4.*Z-3.
      DF2(Z)=4.-8.*Z
      DF3(Z)=4.*Z-1.
c
c   define 1-D basis functions for use at boundary conditions
c
      PH1D(1)=F1(C)
      PH1D(2)=F2(C)
      PH1D(3)=F3(C)
c
```

```
c     define 2-D basis functions in terms of 1-D basis functions
c
      PHI(1)=F1(C)*F1(E)
      PHI(2)=F1(C)*F2(E)
      PHI(3)=F1(C)*F3(E)
      PHI(4)=F2(C)*F1(E)
      PHI(5)=F2(C)*F2(E)
      PHI(6)=F2(C)*F3(E)
      PHI(7)=F3(C)*F1(E)
      PHI(8)=F3(C)*F2(E)
      PHI(9)=F3(C)*F3(E)
c
c     derivatives of 2-D basis functions
c
      PHIC(1)=DF1(C)*F1(E)
      PHIC(2)=DF1(C)*F2(E)
      PHIC(3)=DF1(C)*F3(E)
      PHIC(4)=DF2(C)*F1(E)
      PHIC(5)=DF2(C)*F2(E)
      PHIC(6)=DF2(C)*F3(E)
      PHIC(7)=DF3(C)*F1(E)
      PHIC(8)=DF3(C)*F2(E)
      PHIC(9)=DF3(C)*F3(E)
      PHIE(1)=F1(C)*DF1(E)
      PHIE(2)=F1(C)*DF2(E)
      PHIE(3)=F1(C)*DF3(E)
      PHIE(4)=F2(C)*DF1(E)
```

```
      PHIE(5)=F2(C)*DF2(E)

      PHIE(6)=F2(C)*DF3(E)

      PHIE(7)=F3(C)*DF1(E)

      PHIE(8)=F3(C)*DF2(E)

      PHIE(9)=F3(C)*DF3(E)

      RETURN

      END

      c
*********************************************************************

      c

      c
*********************************************************************

      c

      c THIS SUBROUTINE CALCULATES THE X AND Y COODINATES FOR A
RECTANGULAR

      c AREA HAVING AN X VALUE OF "XLCRD" ON ITS LEFT SIDE AND A Y
VALUE

      c OF "YBCRD" ON ITS BOTTOM FACE

      c

      c
*********************************************************************

      c

      SUBROUTINE
RECTG(NN,NNY,DXR,DYR,XLNGTH,XLCRD,YBCRD,XPT,XR,YR)

      DIMENSION XR(1089),XPT(1089),YR(1089)

      REAL*8 DXR(60),DYR(4)

      c CALCULATE THE X VALUES AT EACH POSITION

      DO 100 I=1,NNY

      XR(I)=XLCRD

      XPT(I)=XR(I)*XLNGTH
```

```
      DO 100 J=(I+NNY),(NN-NNY+I),NNY
      NXL=((J-I)/NNY+1)/2
      XR(J)=XR(J-NNY)+0.5*DXR(NXL)
100   XPT(J)=XR(J)*XLNGTH
c     CALCULATE THE Y VALUES AT EACH POSITIONS
      DO 101 I=1,(NN-NNY+1),NNY
      YR(I)=YBCRD
      DO 101 J=(I+1),(I+NNY-1)
      NYL=(J-I+1)/2
101   YR(J)=YR(J-1)+0.5*DYR(NYL)
      RETURN
      END
```

Appendix III: Mass-transfer Model

Set forth in this appendix is the code used to model the mass-transfer processes taking place within the model pore. The finite difference technique known as alternating direction implicit (ADI) was used. The diffusion equation was solved for each species and the concentration profiles as well as concentration gradients and gaussian-weighted beam deflection was generated. The code was written in Fortran 77 and compiled and ran on a DEC 6420 computer.

```
Implicit Real*8 (a-h,o-z)
Parameter (Xarray=601,Yarray=50)
Real*8 io,zk,iavg,lngth,kp,Itot,hght
 Real*8 Q(Xarray,21),QZ(Xarray,21),QO(Xarray,21),Qstar(Xarray,21)
  Real*8 Ax(Xarray),Bx(Xarray),Cx(Xarray),D(Xarray),R(Xarray)
Real*8 Ay(21),By(21),Cy(21),Dyy(21),Ry(21)
Real*8 cyderv(8,2000),cxderv(8,2000),Dx(Xarray)
  Real*8 cur(Xarray),Curt(Xarray),DE(Xarray),mig(Xarray)
 Real*8 xpt(Xarray),XR(Xarray),PD(10),PC(10)
Dimension ND(10), NC(10)
character*2 pp
  open(unit=5,file='data3.dat',status='unknown')
  open(unit=10,file='xcon4.out',status='unknown')
  open(unit=11,file='ycon4.out',status='unknown')
  open(unit=15,file='curr4.out',status='unknown')
  open(unit=25,file='xderv4.out',status='unknown')
```

```
      open(unit=26,file='yderv4.out',status='unknown')
      open(unit=27,file='dxr4.out',status='unknown')
      open(unit=28,file='dyr4.out',status='unknown')
c
c     ***********************************************************************
c     Input Parameters from data3.dat file
c     ***********************************************************************
c     first line -   height,width,length of cell, ex. curr.dens.,condctvity,
c                    temperature.
c     second line - Initial concentrations, Diffusivities, transfer
c                   coeffs, total current, total time of run.
c     third line -   N = total x-direction spatial mesh points;
c                   M = total y-direction spatial mesh points;
c                   L = number of time mesh points
c     fourth line - NXD = number of positions (XR) at which
c                   derivatives are calculated
c                   NTC = number of times at which conc. profiles are
c                   recorded
c                       tmoc= the time (sec) to open circuit
c                       bp  = position of beam - fraction of height (0 to 1)
c     fifth line -     PD(i) = list of dimensionless positions (XR) (no more than
c                       NXD) at which derivatives are calculated
c     sixth line -  PC(i) = list of times (seconds)  (no more than NTC)
c                       at which concentration profiles are recorded
c     ***********************************************************************
c
      Read (5,*) hght,wdth,lngth,io,zk,temp
```

```
      Read (5,*) cOH,cZn,DZn,DOH,tOH,tZn,Itot,time
      Read (5,*) N,M,L
      Read (5,*) NXD,NTC,tmoc,bp
      Read (5,*) (PD(i), i=1,NXD)
      Read (5,*) (PC(i), i=1,NTC)
 50   Format (3f11.6)
c
c     set general dimensions
c
      write(15,50)N*1.
      iskip=0
      tmax=time
      NIOC=(tmoc/tmax)*L+1
      NSTART=(45/tmax)*L+1
      xmax=2.142857*lngth
      we=lngth
      ce=xmax-lngth
      JW=(we/xmax)*N
      JC=(ce/xmax)*N
      ymax=hght
      do 350 j=1,N-1
350   Dx(j)=xmax/(N-1)
      xpt(1)=0.0
      XR(1)=0.0
      do 351 mm=2,N
      xpt(mm)=xpt(mm-1)+Dx(mm-1)
351   XR(mm)=xpt(mm)/we
```

```
      Dy=ymax/(M-1)
      Dt=tmax/L
      do 805 i=1,NXD
805     ND(i)=(PD(i)*we/Dx(1))+1
      do 806 i=1,NTC
806     NC(i)=(PC(i)*L)/tmax
c
c     Input the current distribution along the bottom of the
c      cell.  This will be used to obtain flux boundary conditions.
c
c     set secondary current distribution - Slot Profile
c
      write(15,50)N*1.
      iavg=Itot/(wdth*lngth)
      io=0.0015
       gnu=sqrt(io*2.*96485.0/(zk*8.31439*temp*hght))*lngth
      do 90, j=1,N
      Curt(j)=0.0
      if(j.gt.JW) go to 91
        Curt(j)=gnu*(exp(gnu*XR(j))+exp(-gnu*XR(j)))
     1      /(exp(gnu)-exp(-gnu))*iavg
      Go To 90
 91   Continue
      if (j.lt.JC) go to 90
      io=0.0005
       gnu=sqrt(io*2.*96485.0/(zk*8.31439*temp*hght))*lngth
        Curt(j)=(-1)*gnu*(exp(gnu*XR(N-j+1))+exp(-gnu*
```

```
     1 XR(N-j+1)))/(exp(gnu)-exp(-gnu))*iavg
 90  continue
    do 92 j=1,N,20
 92  Write(15,50) xpt(j),Curt(j)
c
c    set initial conditions
    do 100 k=1,M
    do 200 j=1,N
     QZ(j,k)=cZn
     QO(j,k)=cOH
     Q(j,k)=0.0
     Qstar(j,k)=0.0
200  continue
100  continue
c
c   Set conc.out t-graph parameters
c
111   Format(1x,'title text is "Dimensionless Concentration"
    1 "x profiles".')
112   Format(1x,'xl is "XR distance".')
113   Format(1x,'yl is "Conc. (C/C0)".')
211   Format(1x,'title text is "Dimensionless Concentration"
    1 "y profiles".')
212   Format(1x,'yl is "YR distance".')
213   Format(1x,'xl is "Conc. (C/C0)".')
114   Format(1x,'page-border is 0.')
115   Format(1x,'legend text is " ".')
```

```
116   Format(1x,'legend units are plot%.')
117   Format(1x,'legend box is 0.')
118   Format(1x,'legend x origin is 80.')
119   Format(1x,'legend y origin is 50.')
120   Format(1x,'input data.')
      Write (10,111)
      Write (10,112)
      Write (10,113)
      Write (10,114)
      Write (10,115)
      Write (10,116)
      Write (10,117)
      Write (10,118)
      Write (10,119)
      Write (10,120)
      Write (11,211)
      Write (11,212)
      Write (11,213)
      Write (11,114)
      Write (11,115)
      Write (11,116)
      Write (11,117)
      Write (11,118)
      Write (11,119)
      Write (11,120)
c
c     begin marching
```

```
      do 500 lt=1,L
c
c     determine if open circuit
c
      if (lt .gt. NSTART) go to 199
197   if (iskip .eq. 1 .or. iskip .eq. 3) go to 198
      do 196 j=1,N
196   cur(j)=0.0
      iskip=1+iskip
      go to 198
199   if (lt .gt. NIOC) go to 197
      if (iskip .eq. 2) go to 198
      do 195 j=1,N
195   cur(j)=Curt(j)
      iskip=1+iskip
198   continue
c
c
c     choose OH or Zincate
c
      do 93 i=1,2
      if (i.eq.2) go to 94
      Diff=DZn
       Diffzc=DZn*1.004e-5/(3.*1.004e-5-2.*DZn)
      trnsf=tZn
      trnsf=0.0
      zi=-2.0
```

```
c
c    Set zincate dc/dy at electrode  =  si*i(x)/n*F*D
c    Reset solution matrix
c
     do 95 j=1,N
     do 98 k=1,M
 98    Q(j,k)=QZ(j,k)
 95     DE(j)=((-1.)*1000./(2.*96487.*Diff))*cur(j)
     go to 96
 94   Diff=DOH
      Diffbc=2.7e-5
      trnsf=tOH
      trnsf=0.0
      zi=-1.0
c
c    Set OH dc/dy at electrode
c    Reset solution matrix
c
     do 97 j=1,N
     do 99 k=1,M
 99    Q(j,k)=QO(j,k)
       tk=(cZn+cOH)*1.004e-5/(QO(j,k)*2.7e-5+(cZn+cOH)*1.004e-5
    1  +4.*QZ(j,k)*DZn)
 97     DE(j)=(1000.*2.*tk/(96487.*Diff))*cur(j)
 96   continue
c
c     set finite difference dimensionless parameters
```

```
      betax=Dt*Diff/(2.0*Dx(1)*Dx(1))
      betay=Dt*Diff/(2.0*Dy*Dy)
c
c     set migration component of mass balance
      do 850 j=1,N
850      mig(j)=(Dt)*(trnsf*iavg*cur(j)*1000.0)/
     1      (zi*96487.0*ymax)
c
c     initialize x coefficient matrix
      do 300 j=2,N-1
      Ax(j)=(-betax)
      Bx(j)=(1.0+2.0*betax)
      Cx(j)=(-betax)
300   continue
      Ax(1)=0.0
      Bx(1)=(1.0+2.0*betax)
      Cx(1)=(-2.0*betax)
      Ax(N)=(-2.0*betax)
      Bx(N)=(1.0+2.0*betax)
      Cx(N)=0.0
c
c     initialize y coefficient matrix
      do 400 k=2,M-1
      Ay(k)=(-betay)
      By(k)=(1.0+2.0*betay)
      Cy(k)=(-betay)
400   continue
```

```
      Ay(1)=0.0
      By(1)=(1.0+2.0*betay)
      Cy(1)=(-2.0*betay)
      Ay(M)=(-2.0*betay)
      By(M)=(1.0+2.0*betay)
      Cy(M)=0.0
c
c     calculate x profiles at star time step
c     set answer vector values
      do 600 k=1,M
      if (k .eq. 1) go to 1
      if (k .eq. M) go to 2
      do 700 j=1,N
        D(j)=betay*Q(j,k+1)-(2.0*betay-1.0)*Q(j,k)+betay*Q(j,k-1)
     1    -mig(j)
700   continue
       call TRIDAG(1,N,Ax,Bx,Cx,D,R)
      do 800 j=1,N
       Qstar(j,k)=R(j)
800   continue
      go to 3
1     do 900 j=1,N
       D(j)=2.0*betay*Q(j,2)-(2.0*betay-1.0)*Q(j,1)-
     1     2.0*betay*Dy*DE(j)-mig(j)
900   continue
      go to 700
2     do 101 j=1,N
```

```
      D(j)=2.0*betay*Q(j,M-1)-(2.0*betay-1.0)*Q(j,M)
     1    -mig(j)
101   continue
      go to 700
3     continue
600   continue
c
c     calculate y profile at present time step
c
      do 201 j=1,N
      if (j .eq. 1) go to 4
      if (j .eq. N) go to 5
      do 301 k=2,M
        Dyy(k)=betax*Qstar(j+1,k)+(1.0-2.0*betax)*Qstar(j,k)
     1    +betax*Qstar(j-1,k)-mig(j)
301   continue
       Dyy(1)=betax*Qstar(j+1,1)+(1.0-2.0*betax)*Qstar(j,1)
     1    +betax*Qstar(j-1,1)-betay*2.0*Dy*DE(j)-mig(j)
6     call TRIDAY(1,M,Ay,By,Cy,Dyy,Ry)
      if (i.eq.2) go to 402
      do 401 k=1,M
401     QZ(j,k)=Ry(k)
      go to 7
402   do 403 k=1,M
403     QO(j,k)=Ry(k)
      go to 7
4     do 501 k=2,M
```

```
      Dyy(k)=2.0*betax*Qstar(2,k)+(1.0-2.0*betax)*Qstar(1,k)
     1    -mig(j)
501   continue
      Dyy(1)=2.0*betax*Qstar(2,1)+(1.0-2.0*betax)*Qstar(1,1)
     1    -betay*2.0*Dy*DE(1)-mig(j)
     go to 6
5     do 601 k=2,M
      Dyy(k)=(1.0-2.0*betax)*Qstar(N,k)+2.0*betax*Qstar(N-1,k)
     1    -mig(j)
601   continue
      Dyy(1)=(1.0-2.0*betax)*Qstar(N,1)+2.0*betax*Qstar(N-1,1)
     1    -betay*2.0*Dy*DE(N)-mig(j)
     go to 6
7     continue
201   continue
93    continue
c
c     conc.output
c
      do 134 kk=1,NTC
134   if (lt.eq.NC(kk)) go to 135
     go to 144
135   t=lt*Dt
      Write (10,136) t
136     format(1x,'"Zincate; y=0.5(d) t=',f7.2,'".')
     do 137 j=1,N,5
      con=QZ(j,M/2)/cZn
```

```
137   Write (10,50) XR(j),con
      Write (11,236) t
236     format(1x,'"Zincate; XR=0.75  t=',f7.2,'".')
      j=1+0.75*we/Dx(1)
      do 237 k=1,M
        YR=(k-1)*Dy/ymax
        con=QZ(j,k)/cZn
237   Write (11,50) con,YR
145   Write (10,140)t
140     format(1x,'"Hydroxide; y=0.5(d)  t=',f7.2,'".')
      do 141 j=1,N,5
        con=QO(j,M/2)/cOH
141   Write (10,50) XR(j),con
      Write (11,240)t
240     format(1x,'"Hydroxide; XR=0.75  t=',f7.2,'".')
      j=1+0.75*we/Dx(1)
      do 241 k=1,M
        YR=(k-1)*Dy/ymax
        con=QO(j,k)/cOH
241   Write (11,50) con,YR
144   continue
c
c     calculate derivatives and refractive index gradients
c     calculate centroid of gradients weighted by Gaussian beam
c           intensity distribution
c     1/e**2 radius (gr) used for our HeNe beam is 50 microns (0.005 cm)
c     integration conducted over a rectangular beam with
```

```
c          sides of length 4*r and ymax
c
c    initialize parameters
     IDXR=0
     kbp=bp*M+1
     gr=0.004
       ixrad=gr*(N-1)/xmax
c    loop over probe beam positions
     go to 520
521  IDXR=1
     do 510 jbp=1,N,5
     go to 522
520  do 510 kk=1,NXD
     jbp=ND(kk)
c    y loop
522  ict=0
     sdx=0.0
     sdy=0.0
     sintn=0.0
     sbintn=0.0
     wdndx=0.0
     wdndy=0.0
     do 511 k=2,M-1
     tswdx=wdndx
     tswdy=wdndy
     tswint=bintn
c    x loop
```

```
      icount=0
      swdndx=0.0
      swdndy=0.0
      sbintn=0.0
      if (ixrad .eq. 0) go to 512
       do 513 j=(jbp-2*ixrad),(jbp+2*ixrad)
      if (j .lt. 2) go to 513
      if (j .gt. N-1) go to 513
      twdndx=wdndx
      twdndy=wdndy
      tbintn=bintn
      go to 514
512   j=jbp
514   continue
c
c     calculate dn/dx and dn/dy at each position on the probe beam
c
        xderv1=(QZ(j+1,k)-QZ(j-1,k))/(2*Dx(1))
        xderv2=(QO(j+1,k)-QO(j-1,k))/(2*Dx(1))
      psi1=0.01899948318+0.0071312*QZ(j,k)
     1 -0.0031386*QZ(j,k)**2
      psi2=0.0106448-0.0008250766*QO(j,k)
     1 +3.1092204e-5*QO(j,k)**2
        yderv1=(QZ(j,k+1)-QZ(j,k-1))/(2*Dy)
        yderv2=(QO(j,k+1)-QO(j,k-1))/(2*Dy)
      dndx=psi1*xderv1+psi2*xderv2
      dndy=psi1*yderv1+psi2*yderv2
```

```
c
c   calculate beam intensity at each position on the probe beam
c       ignoring the Io factor
c   this is the weighting factor for integration over the beam area
c
      x=(j-1)*Dx(1)
      x0=(jbp-1)*Dx(1)
      y=(k-1)*Dy
      y0=bp*ymax
        bintn=exp(-2*((x-x0)**2+(y-y0)**2)/(gr**2))
c
c   calculate the weighted gradients
c
      wdndx=dndx*bintn
      wdndy=dndy*bintn
c
c   back to main part of x loop
c   integrate over x direction
      if (ixrad .eq. 0) go to 515
      if (icount .lt. 1) go to 516
        swdndx=swdndx+0.5*(wdndx+twdndx)*Dx(1)
        swdndy=swdndy+0.5*(wdndy+twdndy)*Dx(1)
        sbintn=sbintn+0.5*(bintn+tbintn)*Dx(1)
516   icount=icount+1
c   end x loop
513   continue
c   rename certain results for y integration
```

```
      wdndx=swdndx
      wdndy=swdndy
      bintn=sbintn
515   continue
c     integrate over y direction
      if (ict .lt. 1) go to 517
       sdx=sdx+0.5*(wdndx+tswdx)*Dy
       sdy=sdy+0.5*(wdndy+tswdy)*Dy
       sintn=sintn+0.5*(bintn+tswint)*Dy
517   ict=ict+1
c     end y loop
511   continue
c     obtain final weighted averages
      if (IDXR .eq. 1) go to 523
       cxderv(kk,lt)=sdx/sintn
       cyderv(kk,lt)=sdy/sintn
     go to 510
523    write(27,50) XR(jbp),sdx/sintn
      write(28,50) XR(jbp),sdy/sintn
c     exit to end of beam positions loop
510   continue
      if (IDXR .eq. 1) go to 500
      if (lt .eq. 83) go to 521
c
c     finish off time steps
c
500   continue
```

```
c     ****************************************************************
c     DERV.OUT  Telegraph Format
c     ****************************************************************
      Write(25,121)
121   Format(1x,'title text is
     1      "Refractive Index Gradients (x dir.)".')
      Write(26,221)
221   Format(1x,'title text is
     1      "Refractive Index Gradients (y dir.)".')
      Write(25,122)
      Write(26,122)
122   Format(1x,'title style is Swiss Medium.')
      Write(25,123)
      Write(26,123)
123   Format(1x,'xl is "time (seconds)".')
      Write(25,124)
124   Format(1x,'yl is "dn/dx (cm)<e.5h.8)-1<exhx)".')
      Write(26,224)
224   Format(1x,'yl is "dn/dy (cm)<e.5h.8)-1<exhx)".')
      Write(25,125)
      Write(26,125)
125   Format(1x,'page-border is 0.')
      Write(25,126)
      Write(26,126)
126   Format(1x,'legend text is " ".')
      Write(25,127)
      Write(26,127)
```

```
127   Format(1x,'input data.')
      do 227 kk=1,NXD
        dimX=(ND(kk)-1.)/(JW-1.)
      Write(25,128) dimX
      Write(26,128) dimX
128     Format(1x,'"XR=',f4.2,'".')
      Write(25,50)0.0,0.0
      Write(26,50)0.0,0.0
      do 129, lt=1,L
      t=lt*Dt
      Write (25,50) t, cxderv(kk,lt)
      Write (26,50) t, cyderv(kk,lt)
129   Continue
227   Continue
      Write(25,130)
      Write(26,130)
      Write(10,130)
      Write(11,130)
130   Format(1x,'end data.')
      Write(25,131)
      Write(26,131)
      Write(10,131)
      Write(11,131)
131   Format(1x,'For every curve.')
      Write(25,132)
      Write(26,132)
      Write(10,132)
```

```
      Write(11,132)
132   Format(1x,'curve thickness is 1.')
      Write(25,133)
      Write(26,133)
      Write(10,133)
      Write(11,133)
133   Format(1x,'message angle is 90.')
      Write(25,160)
      Write(26,160)
      Write(10,160)
      Write(11,160)
160   Format(1x,'message x is .2.')
      Write(25,161)
      Write(26,161)
      Write(11,161)
      Write(10,161)
161   Format(1x,'message text is "bc".')
      Write(25,162)
      Write(26,162)
      Write(10,162)
      Write(11,162)
162   Format(1x,'**file**')
*****************************************************************
      stop
      end
c
      SUBROUTINE TRIDAG (IF,L,A,B,C,D,V)
```

```
      Parameter (Xarray=601,Yarray=50)
      REAL*8 A(1),B(1),C(1),D(1)
       REAL*8 V(1),BETA(Xarray),GAMMA(Xarray)
50    Format (3f11.6)
C     COMPUTE INTERMEDIATE ARRAYS BETA AND GAMMA
      BETA(IF)=B(IF)
       GAMMA(IF)=D(IF)/BETA(IF)
      IFP1=IF+1
      DO 1 I=IFP1,L
       BETA(I)=B(I)-A(I)*C(I-1)/BETA(I-1)
 1     GAMMA(I) = (D(I)-A(I)*GAMMA(I-1))/BETA(I)
C     COMPUTE FINAL SOLN VECTOR V
      V(L)=GAMMA(L)
      LAST=L-IF
      DO 2 K=1,LAST
      I=L-K
 2     V(I)=GAMMA(I)-C(I)*V(I+1)/BETA(I)
      RETURN
      END
c
       SUBROUTINE TRIDAY (IF,L,A,B,C,D,V)
      REAL*8 A(1),B(1),C(1),D(1)
       REAL*8 V(1),BETA(21),GAMMA(21)
C     COMPUTE INTERMEDIATE ARRAYS BETA AND GAMMA
      BETA(IF)=B(IF)
       GAMMA(IF)=D(IF)/BETA(IF)
      IFP1=IF+1
```

```
      DO 1 I=IFP1,L
        BETA(I)=B(I)-A(I)*C(I-1)/BETA(I-1)
1       GAMMA(I) = (D(I)-A(I)*GAMMA(I-1))/BETA(I)
C     COMPUTE FINAL SOLN VECTOR V
       V(L)=GAMMA(L)
       LAST=L-IF
       DO 2 K=1,LAST
       I=L-K
2       V(I)=GAMMA(I)-C(I)*V(I+1)/BETA(I)
       RETURN
       END
```

LAWRENCE BERKELEY LABORATORY
UNIVERSITY OF CALIFORNIA
INFORMATION RESOURCES DEPARTMENT
BERKELEY, CALIFORNIA 94720